01 May 2023

# Tensile Behavior of Layered Rock Disks under Diametral Loading: Experimental and Numerical Investigations

Mostafa Asadizadeh

Saeed Khosravi

Soheil Abharian

Mehrdad Imani

*et. al. For a complete list of authors, see* https://scholarsmine.mst.edu/min_nuceng_facwork/1711

## Recommended Citation

**ORIGINAL PAPER**

# Tensile behavior of layered rock disks under diametral loading: experimental and numerical investigations

Mostafa Asadizadeh[1] · Saeed Khosravi[2] · Soheil Abharian[3] · Mehrdad Imani[1] · Jamshid shakeri[4] · Ahmadreza Hedayat[1] · Nima Babanouri[4] · Taghi Sherizadeh[5]

## Abstract

The tensile strength and cracking behavior of layered rocks in a tensile stress field are one of the most significant characteristics of rock masses, which may strongly affect the stability of rock structures. The study presented here investigated the effect of layer spacing and inclination angle on the indirect tensile strength, crack development, failure pattern, and contact force chain of layered disks under diametral loading using experimental and numerical investigations. Numerous experimental models made from plaster were examined under diametral loading, and a two-dimensional Particle Flow Code (PFC$^{2D}$) was adopted for in depth simulation of the failure process. Both numerical and experimental results were found to be in great agreement and showed that the increase in the layer orientation up to 15° results in the peak in the tensile strength followed by a decrease. Specimens with the spacing ratio (SR) of 0.5 and 0.1 showed the highest and lowest tensile and compressive stresses at the disk center, respectively. Moreover, the numerical analysis indicated the formation of three failure pattern types: *TL*, *PB*, and *TL-PB*. Tensile cracks mainly formed in the direction of diametral loading, and their maximum number formed at 15° and SR = 0.5. Additionally, the shear ones formed in a conjugate system and had negligible numbers. The analysis of the contact force chain showed that the layers do not affect the compressive force chain at $\alpha < 45°$ but at higher angles, the stronger layers transfer compressive force. However, when α ranges from 0° to 30°, tensile forces are distributed in stronger layers, and with an increase in $\alpha$, the concentration of these forces in these layers diminishes and the forces are reoriented in the direction of diametral loading.

**Keywords** Layered rock · Diametral loading · Indirect tensile strength · Crack development · Contact force chain · PFC$^{2D}$

## Abbreviations

| | |
|---|---|
| ISRM | International society for rock mechanics |
| TL | Through layer fracture pattern |
| PB | Parallel to layer fracture pattern |
| TL-PB | Mixed fracture pattern |
| PFC | Particle flow code |
| FJ-BPM | Flat-jointed bonded-particle model |
| DEM | Discrete element method |
| SR | Spacing ratio |

## List of symbols

| | |
|---|---|
| UCS | Uniaxial compressive strength (MPa) |
| $E$ | Modulus of elasticity (GPa) |
| $\sigma_t$ | Tensile strength (MPa) |
| $\nu$ | Poisson's ratio |
| $\underline{E}_c$ | Particle modulus of elasticity (GPa) |
| $\overline{\lambda}$ | Radius multiplier |
| $\varphi_{Fj}$ | Friction coefficient of flat-joint bonds |
| $\sigma_t\text{-}Fj$ | Tensile strength of flat-joint bonds (MPa) |
| $c_{Fj}$ | Cohesion coefficient of flat-joint bonds (MPa) |
| $t_l$ | Thickness of the layers (mm) |
| $t$ | Disk thickness (mm) |
| $\overline{E}_c$ | Elastic modulus of flat-joint bonds (GPa) |
| $k_n$ | Normal stiffness of ball contacts (N/m) |

✉ Mostafa Asadizadeh
  masadizadeh@mines.edu

1   Colorado School of Mines, 1500 Illinois St, Golden, CO 80401, USA

2   Department of Mining Engineering, Shahid Bahonar University of Kerman, Kerman, Iran

3   Department of Civil and Environmental Engineering, Western University, London, ON, Canada

4   Department of Mining Engineering, Hamedan University of Technology, Mardom Street, Hamedan 65155-579, Iran

5   Department of Mining and Explosives Engineering, Missouri University of Science and Technology, Rolla, MO 65409, USA

| | |
|---|---|
| $k_s$ | Shear stiffness of ball contacts (N/m) |
| $R_{max}$ | Maximum radius of balls (mm) |
| $R_{min}$ | Minimum radius of balls (mm) |
| $\bar{k}_s$ | Shear stiffness of flat-joint bonds (N/m) |
| $\bar{k}_n$ | Normal stiffness of flat-joint bonds (N/m) |
| $\sigma_{xx}, \sigma_{yy}, \sigma_{xy}$ | Stress tensor components in global coordinate x,y (MPa) |
| $\alpha$ | Layer inclination angle (°) |
| $D$ | Disk diameter (mm) |
| $P$ | Applied load at the failure of the disk (N) |

# 1 Introduction

Investigation of the tensile strength of rocks is of paramount importance since this property can govern the mechanical behavior and failure mechanism of rock structures such as slopes, pillars, and tunnels. A crucial factor affecting the tensile behavior of rocks is anisotropy. Rocks are generally anisotropic, predominantly stemming from discontinuities such as schistosity, joints, and bedding planes [3]. Anisotropy may adversely affect the tensile strength of rocks [1], and if this is overlooked in the design of the structures built within rocks, depending on the extent of anisotropy, serious challenges may arise in various scales [4, 14].

Due to the inherent difficulties associated with the direct determination of the tensile strength, it is primarily obtained indirectly [40]. Diametral loading test, due to the ease of sample preparation and the simple test procedure, is the most widely used approach for the determination of the rock tensile strength. In addition to the rock anisotropy, many researchers have investigated factors affecting the tensile strength in diametral loading tests. For instance, the effect of the intermediate principal stress [58, 59], rock heterogeneity [12, 13, 61], contact loading angle, and stress distributions [2, 7, 8, 19, 20, 57], and frictional force between the loading platens and disk-shaped specimens [16, 29, 33] have been studied. The cracking processes in diametrically loaded samples have also been studied [41, 42, 51].

Many researchers have examined the tensile strength of transversely isotropic rocks. Although micro-scale parameters such as porosity, grain size, and mineral content can affect the tensile behavior and fracture pattern of stratified rocks [46], the bedding orientation may exert a significant effect on the tensile strength and fracture mode of such rocks [10, 18, 35].

A few studies have investigated the impact of discontinuity's inclination angle on the tensile strength of layered rocks such as sandstone, shale, and slate and revealed that the tensile strength generally reduces when the inclination angle increases [21, 27, 28, 30, 34, 43, 47, 50, 54, 56, 60]. Tan et al. [45] performed testing on slate specimens subjected to diametral loading and found that the tensile strength decreases when the foliation inclination angle decreases from 0° to 30° and remains roughly unchanged for higher inclination angles.

However, Vervoort et al. [49] identified four distinct trends for tensile strength versus layer inclination angle after an extensive experimental investigation on different anisotropic rocks, including sandstone shale, slates, schist, and gneisses. These trends include almost stable, a plateau for $\alpha < 45°$ then a steady decline, a downward trend, and finally, falling sharply for $\alpha < 45°$ and then a plateau. Moreover, Xu et al. [53] experimentally investigated 23 types of transversely isotropic rocks and introduced five different patterns, including virtually unchanged, an upward trend, stable before 60° and then an upward trend, downward trend for $\alpha$ up to 45°, then a plateau, and finally, U-shaped variation. Xu et al. [52], based on the experimental studies carried out on 20 anisotropic rocks, including schist, sandstone, granite, VRK hornfel, pyrophyllite, gneiss, and coal, established six trends, including: almost stable, a downward trend followed by a plateau, a plateau followed by an upward trend, U-shaped, an upward trend followed by a plateau, and finally an upward trend.

In recent years, thanks to the advent of high-speed computers and the development of numerical methods, researchers have adopted numerical simulation to study the tensile behavior and failure pattern of transversely isotropic rocks under diametral loading conditions. Park et al. [35, 36]evaluated the capability of parallel bond and smooth joint contact models using PFC (2D&3D) for the simulation of the tensile behavior of anisotropic samples subjected to diametral loading. Their findings were consistent with experimental results of both fracture pattern and tensile strength. However, the effect of layer thickness on tensile strength and cracking process and the distribution of tensile and compressive forces in the layers were not investigated in this study. Duan and Kwok [18] used PFC[2D] to assess the possibility of adopting a parallel bond model along with a smooth joint model for the numerical simulation of anisotropic rocks under diametral loading, which showed that weak layers in such rocks could be reasonably simulated by applying the smooth joint contact model. They also concluded that the failure pattern and strength of specimens are affected by the shear-to-normal strength ratio and the stiffness of smooth joints, respectively. However, in their study, flat-joint, bonded-particle model (FJ-BPM) was not adopted, despite some recent studies reporting its success in evaluation of mechanical behavior and simulation of the cracking processes compared to the parallel bond model [6, 44].

Yang and Huang [55] studied the effect of anisotropy induced by joints in sandstone utilizing PFC[2D] and reported that tensile strength peaks at $\alpha = 10°$ and minimizes at

$\alpha = 80°$. Wang et al. [50] examined anisotropy in jointed rock masses by adopting PFC[2D] and experimental investigations on biotite granulite samples and introduced an index named directionality incorporating both anisotropy and spatial variability of the tensile strength. They found that in numerical and experimental investigations, samples with $\alpha = 30°$ and $0°$ have the highest tensile strength. Xu et al. [53] investigated the effect of the rock matrix's micro-structure and bedding plane's strength on the tensile strength using PFC[2D] and found that the proportion of pre-existing cracks and shear strength of the bedding planes greatly influence the tensile strength.

Investigation of the cracking process may provide a better understanding of the failure mechanism under diametral loading. Experimental investigations conducted by Tavallali and Vervoort [48] and Khanlari et al.[27] on sandstone specimens suggested three fracture patterns. The studies showed that for layer inclination angle lower than $45°$, the central fracture is dominant, while for angles higher than $60°$, fractures mainly propagate along the bedding plane. In addition, for inclination angles between $45°$ and $60°$, a mixed pattern occurs. Similarly, Feng et al. [21] reported three patterns based on laboratory experiments on shale. Yang et al. [54] identified three fracture patterns, including arc fracture, central fracture, and a combination of the two.

Liu et al. [32] adopted PFC[2D] to simulate the fracture patterns evolving in the diametral loading test and suggested that three patterns can develop, including splitting across layers ($\alpha = 0°$–$45°$), splitting along layers ($\alpha = 60°$ to $90°$), and combined fracture mode ($\alpha = 75°$). Debecker and Vervoort [15] conducted a numerical investigation on slate specimens using Universal Distinct Element Code (UDEC) and concluded that three fracture patterns occur in diametral loading, including shear cracks near the loading platens along schistosity and through layers for $\alpha \le 20°$, tensile cracks along schistosity for $\alpha \ge 80°$, and shear cracks along schistosity when $\alpha$ ranges between $30°$ and $80°$. Yang and Huang [55] carried out a numerical investigation using PFC[2D] and identified three failure modes, namely tensile failure ($\alpha < 30°$), shear failure ($\alpha = 70°$ and $80°$), and a combination of the two modes ($30° < \alpha < 60°$ and $90°$).

Tan et al. [45] employed Discrete Element Code (DEM) to examine slate discs subjected to diametral loading and found that when the angle between schistosity and loading direction ranges from $0°$ to $45°$, cracks propagate along the bedding plane, for angles of $60°$ and $75°$, mixed patterns occur and for the angle of $90°$, fractures propagate through the schistosity. In fact, when the angle is $0°$ or $90°$, tensile splitting results in failure, whereas for $15°$, $30°$ and $45°$ angles, shear failure along schistosity dominate failure. For $60°$ and $75°$, the combination of tensile splitting and shear failure takes place. He and Afolagboye [22] used PFC[2D] to

study the impact of layer inclination angle and interlayer bond strength of shale and reported higher strength when loading was applied perpendicular than parallel to the lamination planes and identified four groups of fracture patterns, including curved, broken-linear, layer-activated, and central-linear fractures. Their study demonstrated that as interlayer bonding strength increases, the number of microcracks decreases. However, the effect of the spacing ratio of layers on the mechanical and cracking behavior of layered rocks was not explored.

Furthermore, Yang et al. [54] adopted PFC[2D] to simulate the behavior of layered shale samples under diametral loading conditions. The results indicated that tensile cracks occurring within the rock matrix and shear cracks propagating along the bedding plane were responsible for fracturing, and the bedding plane and bonding force existing between layers governed the anisotropic response of shale. Xu et al. [52] investigated the effect of the non-planar microstructure of an anisotropic rock matrix using PFC[2D], which indicated that shear and tensile failure of pre-existing micro cracks primarily led to the evolution of cracks in the rock matrix.

The effect of a sequence of weak and strong layers on tensile behavior, crack development, failure pattern, and force chain distribution of rock samples has not been thoroughly investigated in a combined experimental and numerical study yet. The strength anisotropy of layers may redistribute the force chain in the layers and affect the crack development, and result in a failure pattern [11, 17, 31]. Bedding planes impose high anisotropy in layered rocks and strongly affect failure pattern and stability of rock structures built in/on layered rock mass. Therefore, more investigations are required to explain layered rocks' tensile strength anisotropy and failure mechanism. In this research, several experimental layered disks were made using a mix of plaster and water, and strength anisotropy was implemented by using different mix components. The layers were built using molding techniques in which the upper one covers a lower layer before complete hardening to create specimens made up of alternate weaker and stronger layers. A vast number of laboratory experiments, as well as numerical analyses using PFC[2D], were conducted to investigate the tensile behavior, crack development failure pattern, and force chain distribution in the layered disks subjected to diametral loading.

## 2 Experimental program

In this study, 21 layered disks were made of two mixes made of different combinations of plaster and water. Non-layered samples were also cast to characterize the mechanical properties of the mixtures. Three disks and three cylindrical specimens were prepared for each of the mixtures.

To build the layered disks, a transparent and closed cylindrical mold measuring 50 mm in inner diameter and 150 mm in height was selected and laid horizontally. A longitudinal slot was created on the top side of the mold for pouring the mix into it, and its outer surface was marked to specify the thickness of the layers. Stronger layers (Type 1) were made using plaster and water by a weight ratio of 1.2:1 (plaster to water) in contrast to the other layer (Type 2), which was prepared by a weight ratio of 1:1. These proportions were obtained through a trial-and-error process. The blue color was added to the mixture of stronger layers so that the two types of layers were visually distinguishable (see Fig. 1a).

The setting time was selected such that the penetration of the two mixes into each other and the creation of interlayer joints did not occur. Hence, after 60 s passed the time when either of the mixtures was poured into the mold, the other mixture was cast to make the next upper layer. This process proceeded until the mold filled up completely, which resulted in specimens containing alternate layers of Type 1 and Type 2. The specimens were then removed from the mold and kept at room temperature for 14 days. Finally, the cylindrical specimens were cut into disks of 25 mm thickness required for the diametral loading test (see Fig. 1b). Three groups of specimens were cast with different layer thicknesses equal to 5 mm, 10 mm, and 25 mm. In this study, the spacing ratio (SR) is defined as follows:

$$SR = \frac{t_l}{D} \tag{1}$$

where $t_l$ is the thickness of the layers and $D$ is the disk diameter. Therefore, the values of $SR$ are obtained, including 0.1, 0.2, and 0.5. For each spacing ratio, seven different values of

$\alpha$, including 0°, 15°, 30°, 45°, 60°, 75°, and 90°, were cast and examined.

The casting of non-layered disks and cylindrical specimens followed the same procedure as the layered ones. However, the blue color was not added to the two mixes. After curing the cylindrical specimens, both ends of the three were cut perpendicular to the cylinder's longitudinal axis and then leveled to create a sample measuring 120 mm high and 50 mm in diameter and then subjected to axial loading.

Both uniaxial compressive and diametral loading tests were performed in compliance with the methods suggested by the International Society for Rock Mechanics [25]. Tensile strength is calculated according to the following equation:

$$\sigma_t = \frac{2P}{\pi Dt} = 0.636 \frac{P}{Dt} \tag{2}$$

where $\sigma_t$ is tensile strength, $P$ is the applied load at the failure of the disk, $D$ is disk diameter, and $t$ is disk thickness (see Fig. 2).

## 3 Numerical simulations

In this paper, the Discrete Element Method (DEM) was adopted to investigate the effect of layer geometry on the tensile behavior of disk-shaped specimens. The Flat-jointed bonded-particle model in two-dimensional Particle Flow Code (PFC$^{2D}$) was employed to examine tensile strength, crack development, failure pattern, and force chain in the samples [5, 9, 23, 37].



**Fig.1 a** cast layered samples, **b** layered disks

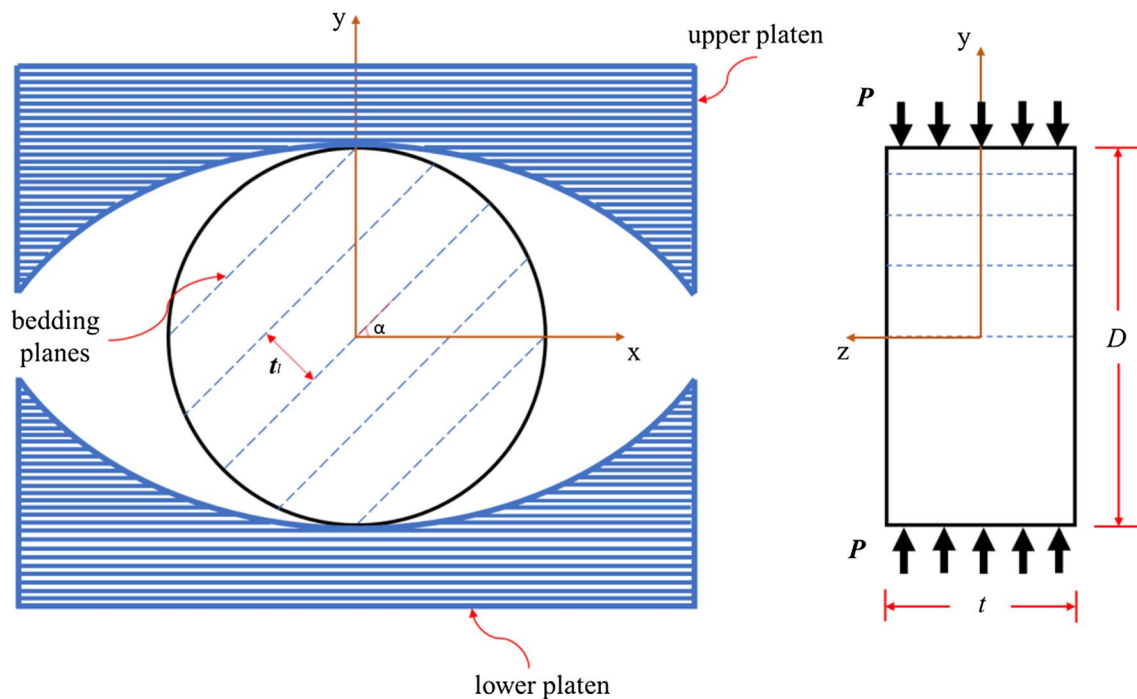a)                                                                    b)
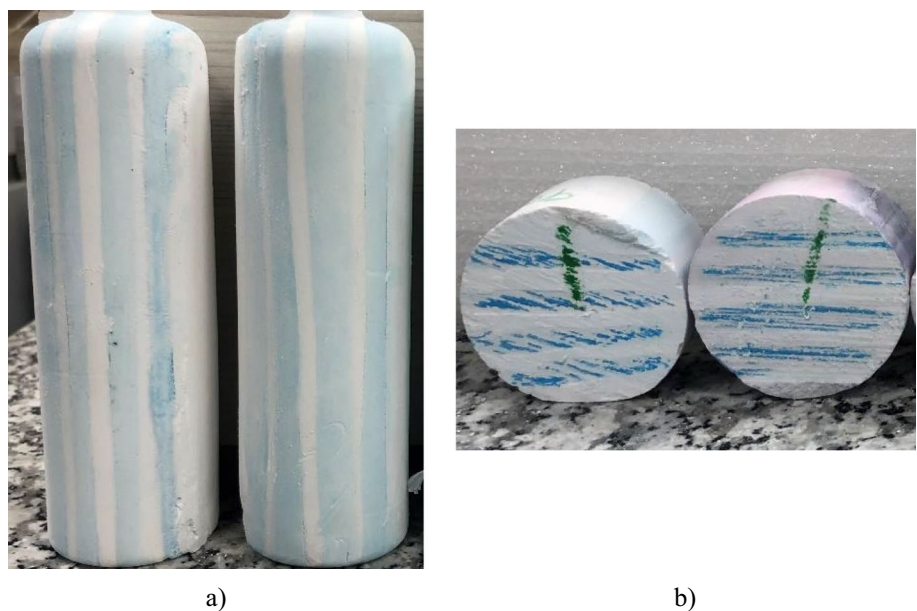
**Fig. 2** Geometrical features of a layered disk

### 3.1 Flat-jointed bonded-particle model

In order to model the intact rock, the flat-jointed bonded-particle model (FJ-BPM) was adopted. This model creates a group of interconnected particles capable of modeling intact materials. In this model, micro-properties of both particles and bonds govern how the assembly responds to various loading conditions. In addition, each contact between two particles simulates the response of an interface with finite length and locally planar virtual surfaces divided into bonded or unbounded elements [38]. These elements can sustain the applied load as long as it does not exceed their bond strength. When a bond fails, micro-cracks initiate, and the stress state is redistributed, all of which result in the bond progressively breaking. When these fractures develop, expand and coalesce, macroscopic cracks appear.

### 3.2 Calibration of flat-joint BPM micro-parameters

Estimating the micro-properties of particles and bonds is not feasible through laboratory experiments, but a trial-and-error process using uniaxial compressive and diametral loading can be employed instead [6, 9, 26]. In such a practice, macro-properties measured in the laboratory are used as boundary conditions to back-calculate the micro-properties in the models. The micro-scale properties of a bonded particle model are commonly calibrated against $UCS$, $E$, $\nu$, and $\sigma_t$ [8, 39], which are obtained from unconfined compression

test and diametral loading test. The first three parameters are calibrated using the results of the uniaxial compressive test. The numerical model had the same dimensions as the laboratory specimens mentioned in Sect. 2 for the uniaxial compressive test and contained two approaching walls to apply the compressive load. $E$, which depends on the particle modulus ($E_c$), the parallel bond modulus $\left(\overline{E}_c\right)$, the particle normal to shear stiffness ratio ($k_n/k_s$), and the parallel bond normal to shear stiffness ratio $\left(\overline{k}_n/\overline{k}_s\right)$, was the first parameter that was calibrated. Then, in an iterative process, $\nu$, which is a function of $k_n/k_s$ and $\overline{k}_n/\overline{k}_s$, was back-calculated. The next calibrated property was $UCS$, dependent on the normal and shear strengths of parallel bonds [6, 9, 24, 39]. The fracture patterns for numerical models and experimental samples are shown in Fig. 3, which reasonably match each other.

The tensile strength is back analyzed by using the results of diametral loading tests. The dimensions of the numerical disks were equal to those of the experimental ones mentioned in Sect. 2. In the simulation stage, a measurement circle with a radius of 15 mm, was defined at the disk center to monitor all two-dimensional stress tensor components during the simulation. The maximum of $\sigma_{xx}$ is reported as $\sigma_t$ of the numerical specimens. This calibration process ultimately led to the final values of $\sigma_{t\text{-}Fj}$, $c_{Fj}$, and $\varphi_{Fj}$, initially obtained in the calibration of $UCS$. The resulting fractures at failure are shown in Fig. 4, which indicates a good agreement

**Fig. 3** A comparison between the final failure patterns obtained from **a** numerical simulation and **b** experimental test of uniaxial compression test for specimens made of Type 1 and Type 2 materials



(a)    (b)

Type 1



(a)    (b)

Type 2
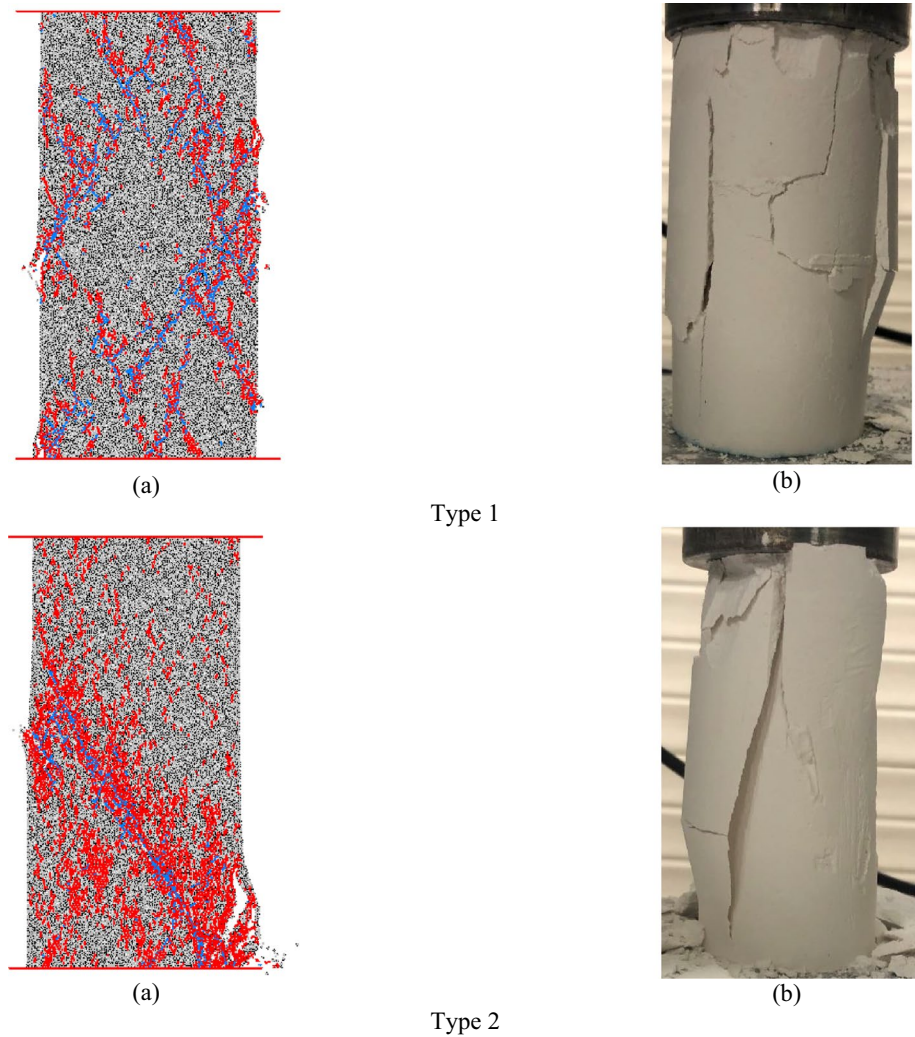
between the results of numerical simulations and laboratory tests.

The final values obtained from the calibration phase are listed in Table 1, where $R_{max}$ is the maximum circle's radius, while $R_{min}$ is the minimum circle's radius. $k_n/k_s$ is the ratio of normal to shear stiffness of ball contacts. $\overline{\lambda}$ is the radius multiplier, $\overline{E}_c$ is the elastic modulus of flat joint bonds, $c_{Fj}$, and $\varphi_{Fj}$ are the tensile strength, cohesion, and friction coefficient of flat joint bonds, respectively. $\overline{k}_n/\overline{k}_s$ is the ratio of the normal stiffness to the shear stiffness of a flat joint bond.

Results of uniaxial compressive and diametral loading tests, calculated from laboratory tests and numerical analyses, are presented in Table 2. As evident, there are marginal differences between these two groups of results.

Finally, the flat-joint model was used for layer contacts, and the micro-parameters of the weaker layer (Type 2 in Table 2) were assigned to the contact.

## 4 Results and discussion

### 4.1 Stress state

#### 4.1.1 Indirect tensile strength ($\sigma_{xx}$)

After obtaining the values of micro-parameters, numerical analyses were conducted using PFC$^{2D}$ to reproduce the experimental diametral loading tests. In the numerical models, $\sigma_{xx}$ represents the tensile strength of the disks. Both numerical and experimental results are presented in Fig. 5. The maximum values of $\sigma_{xx}$ for samples with $SR = 0.1$, 0.2, and 0.5 calculated from numerical simulations were 0.39, 0.40, and 0.54 MPa, and those computed from laboratory experiments were 0.37, 0.43, and 0.51 MPa, respectively. As evident in Fig. 5, the variation of tensile strength in all the specimens followed the same trend with a few slight differences, which matched the second trend introduced by Vervoort et al. [49]. In all the specimens, $\sigma_{xx}$ reached the peak at $\alpha = 15°$, but for higher inclination angles, minor

**Fig. 4** A comparison between the final failure patterns obtained from **a** numerical simulation and **b** experimental test of diametral loading test for specimens made of type 1 and type 2 materials
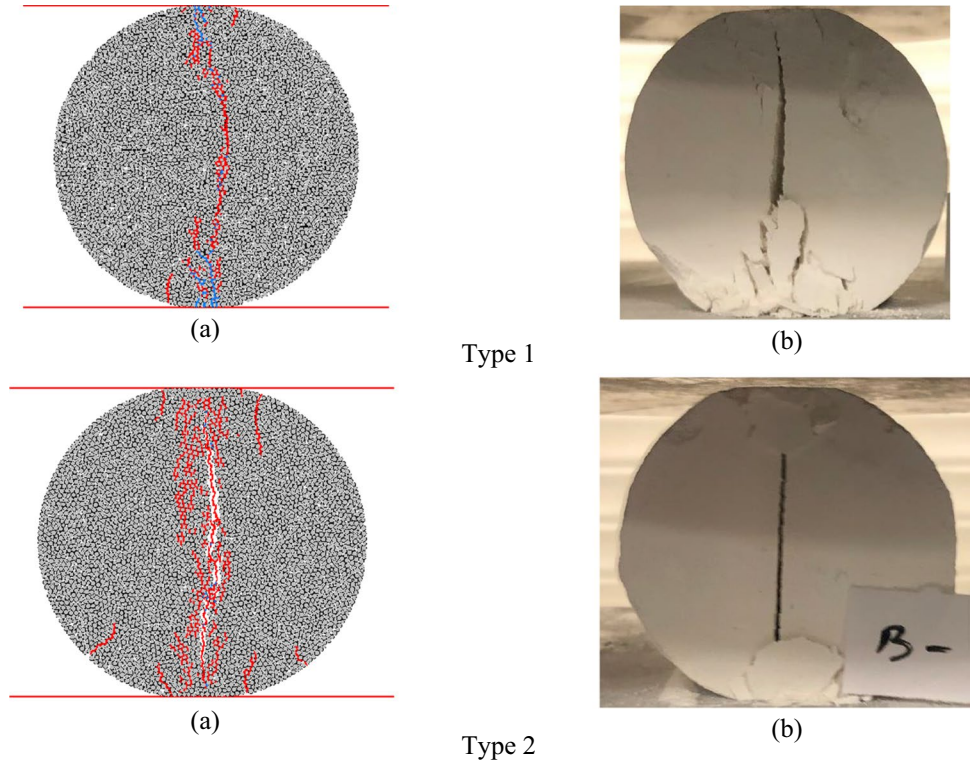


(a)     (b)     Type 1



(a)     (b)     Type 2

**Table 1** Calibrated micro-parameters of the flat-joint BPM

| Balls parameters | Value | |
|---|---|---|
| Material | Type 1 | Type 2 |
| Density (kg/m$^3$) | 1100 | 1040 |
| $R_{min}$(mm) | 2.0 | 2.0 |
| $R_{max}/R_{min}$ | 1.5 | 1.5 |
| Friction coefficient | 0.3 | 0.3 |
| $k_n/k_s$ | 2.1 | 2.1 |
| Falt -join BPM parameters | Value | |
| $\overline{\lambda}$ | 1.0 | 1.0 |
| $\overline{E}_c$ (GPa) | 0.5 | 0.1 |
| $\sigma_{t\text{-Fj}}$ (MPa) | 2.0 | 1.2 |
| $c_{Fj}$ (MPa) | 3.0 | 2.8 |
| $\varphi_{Fj}$ | 0.3 | 0.3 |
| $\overline{k}_n/\overline{k}_s$ | 2.1 | 2.1 |
| Number of elements | 4.0 | 4.0 |

**Table 2** Comparison between the resulting data obtained from laboratory tests and numerical simulations

| Parameter | Experimental | | Numerical | | Error (%) | |
|---|---|---|---|---|---|---|
| Material | Type 1 | Type 2 | Type 1 | Type 2 | Type 1 | Type 2 |
| $\sigma_c$ (MPa) | 6.66 | 5.13 | 6.60 | 5.22 | 1.00 | 1.88 |
| $E$ (GPa) | 0.56 | 0.08 | 0.57 | 0.12 | 3.19 | 0.56 |
| $\nu$ | 0.17 | 0.17 | 0.17 | 0.17 | 0.00 | 0.00 |
| $\sigma_t$(MPa) | 0.56 | 0.13 | 0.56 | 0.13 | 0.00 | 0.00 |
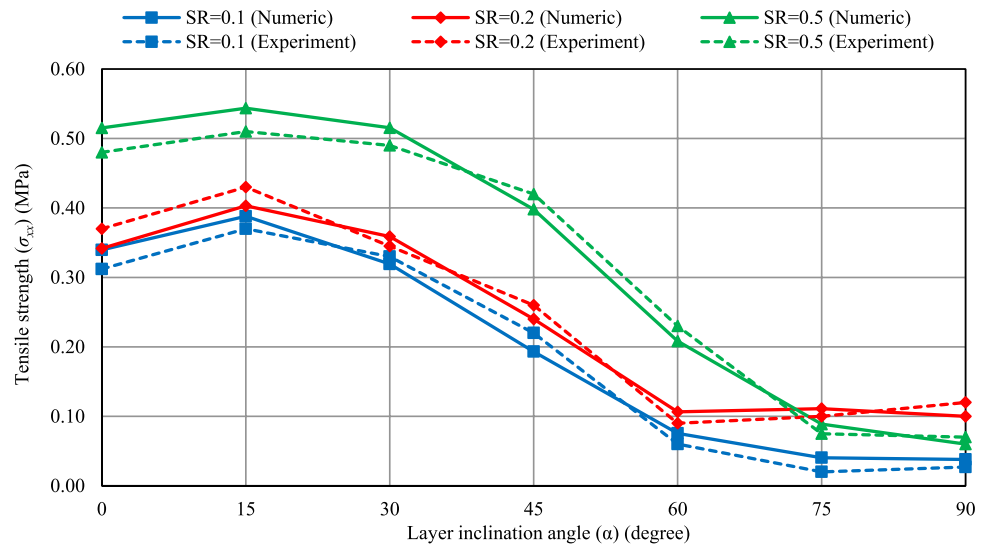
differences were observed. In samples with $SR = 0.1$ and 0.2, $\sigma_{xx}$ dropped significantly with the increase in the inclination angle and reached well below 0.05 MPa at $\alpha = 75°$. However, in samples with $SR = 0.5$, $\sigma_{xx}$ reached the minimum of 0.05 MPa at $\alpha = 90°$. It is noteworthy that disks with $SR = 0.1$ had the lowest values of $\sigma_{xx}$ compared to disks with $SR = 0.2$ and 0.5 over the entire range of layer inclination angle. On the other hand, when $\alpha < 75°$, the highest values of $\sigma_{xx}$ occur in specimens with $SR = 0.5$, while for higher layer inclination angles, the highest values of $\sigma_{xx}$ were seen in samples with $SR = 0.2$.

### 4.1.2 Compressive ($\sigma_{yy}$) and shear ($\sigma_{xy}$) stresses

The variations of compressive ($\sigma_{yy}$) and shear ($\sigma_{xy}$) stresses, measured at the disk center, are shown in Figs. 6 and 7, respectively. Generally, in samples with $SR = 0.1$ compared

to the other two disk groups, the lowest $\sigma_{yy}$ was measured, while those with $SR = 0.5$ had the highest values of this stress component (see Fig. 6). In the former specimens, $\sigma_{yy}$ remained nearly stable at around 1.2 MPa when $\alpha \leq 15°$. It then declined steadily to 0.5 MPa at $\alpha = 75°$ before increasing slightly to about 0.7 MPa at $\alpha = 90°$. For $SR = 0.2$, $\sigma_{yy}$ experienced an increase of around 0.2 MPa from $\alpha = 0°$–15°, after which it fell constantly to 0.7 MPa at $\alpha = 75°$, before reaching to 1.8 MPa at $\alpha = 90°$. This high level of compressive stress may be because of the fact that the central layer acts as a vertical beam and increases the bearing capacity of the samples, and compressive strength increases (see Fig. 9g). The trend of $\sigma_{yy}$ for disks with $SR = 0.5$ is akin to that of those with $SR = 0.2$, and this stress component peaked at around 1.9 MPa at $\alpha = 15°$. However, when $\alpha$ varied from 75° to 90°, unlike disks with $SR = 0.2$, $\sigma_{yy}$ fell slightly from 0.65 MPa to 0.56 MPa.
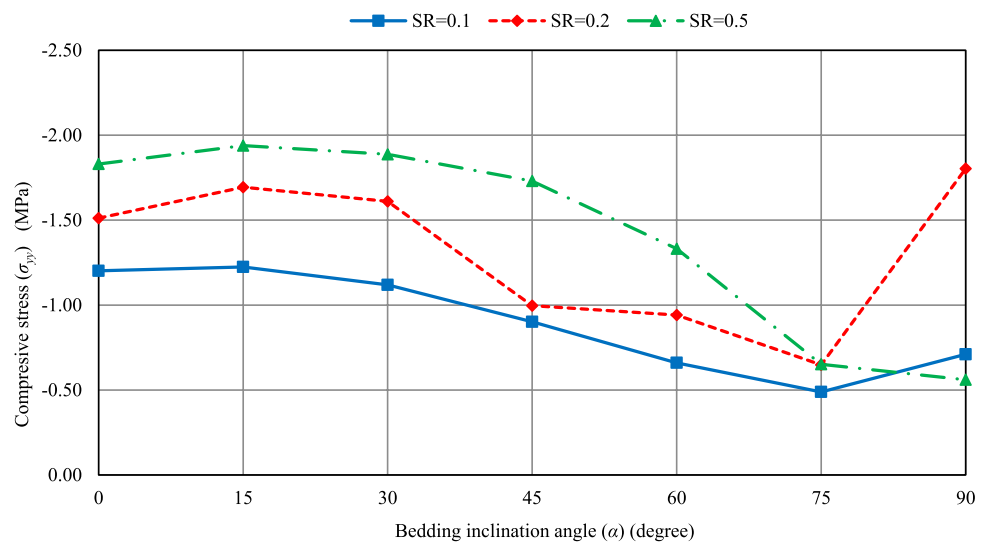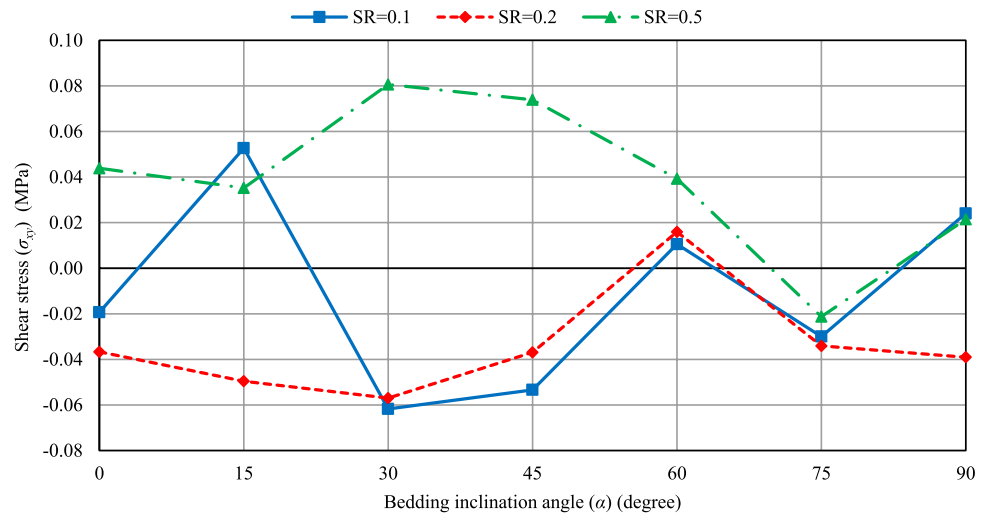
**Fig. 7** Variations of shear stress at the center of the layered disks ($\sigma_{xy}$)



In regards to the shear stress ($\sigma_{xy}$), various trends were observed for the different layer spacing ratios (see Fig. 7). For the samples with $SR = 0.1$, the direction of $\sigma_{xy}$ changed at $\alpha = 15°$, $60°$, and $90°$. Moreover, its magnitude increased from $\alpha = 0°$–$30°$ and peaked at 0.06 MPa. It then declined considerably at $\alpha = 60°$, followed by an increase at $\alpha = 75°$, before falling to nearly 0.02 MPa at $\alpha = 90°$. In the disks with $SR = 0.2$, the direction of shear stress changed at $\alpha = 60°$. In addition, its magnitude rose to 0.06 MPa from $\alpha = 0°$ to $30°$, followed by a noticeable fall at $\alpha = 60°$. Afterward, it went up steadily to about 0.04 MPa at $90°$. Finally, when $SR = 0.5$, a change in the direction of $\sigma_{xy}$ occured at $\alpha = 75°$, and its magnitude peaked at $\alpha = 30°$ (0.08 MPa), which was then followed by a dramatic decrease to 0.02 MPa at $\alpha = 75°$. This value did not change for $\alpha = 90°$. However, the magnitude of shear stress was far lower compared to that of tensile and compressive stresses.

## 4.2 Fracture pattern

The different failure patterns of the three groups of layered disks are presented for both numerical models and laboratory specimens (see Figs. 8, 9 and 10). In these figures, in the numerical models, dark gray and light gray represent Type 1 and Type 2 material, respectively, while in the experimental samples, blue and white are indicative of those layers, respectively. In general, three distinct fracture patterns are recognizable in both numerical and experimental models including: through layer fracture (TL), parallel to bedding plane fracture (PB), and combined fracture pattern (TL–PB). These patterns are consistent with those reported by Tavallali and Vervoort [48], Khanlari et al. [27], Feng et al. [21], and Yang and Huang [55]. It is also noteworthy that TL and the PB occurring at $\alpha = 90°$ are vastly akin to the failure pattern of non-layered specimens [41].

### 4.2.1 Disks with SR = 0.1

For these samples, fracture patterns are shown in Fig. 8. As it can be seen, when $\alpha < 30°$, TL was the primary mode that caused the failure. Additionally, cracks evolved along the disk centerline, although there was a slight difference between the failure surface of $\alpha = 0°$ and $\alpha = 15°$ (see Fig. 8a, b). The failure surface of both samples was formed by cracks propagating along an almost straight line beginning from the contact with the upper platen and ending with the lower platen. Furthermore, the pattern for the other layer inclination angle was classified as PB. There were some micro cracks in this group of samples that did not lead to complete failure of the surface and could not be observed by the naked eye in the experimental samples.

Experimental models for $\alpha = 0°$ showed compaction in the upper and lower weak layers, and the failure pattern differed completely from the numerical one (see Fig. 8a). The fracture patterns of the remaining samples were virtually the same as the numerical models. Therefore, it was inferred that the numerical and experimental simulations were in good agreement.

### 4.2.2 Disks with SR = 0.2

Three fracture patterns were observed in these disks (see Fig. 9). It can be seen from numerical results that when $\alpha = 0°$ and $15°$, the dominant failure pattern was TL (see Fig. 9a, b). The fracture formed a virtually straight line along the disk centerline. However, the pattern for $\alpha = 30°$ and $45°$ are grouped into TL–PB as part of the bedding plane was activated too (see Fig. 9c, d). The length of this part was bigger in the disk with $\alpha = 45°$. Moreover, the pattern for $\alpha = 60°$, $75°$, and $90°$ was PB. However, in disks with $\alpha = 60°$ and $75°$, cracks evolved along the bedding planes, and micro-cracks branched from the major crack into one or

a) α=0°    b) α=15°    c) α=30°    d) α=45°



e) α=60°    f) α=75°    g) α=90°

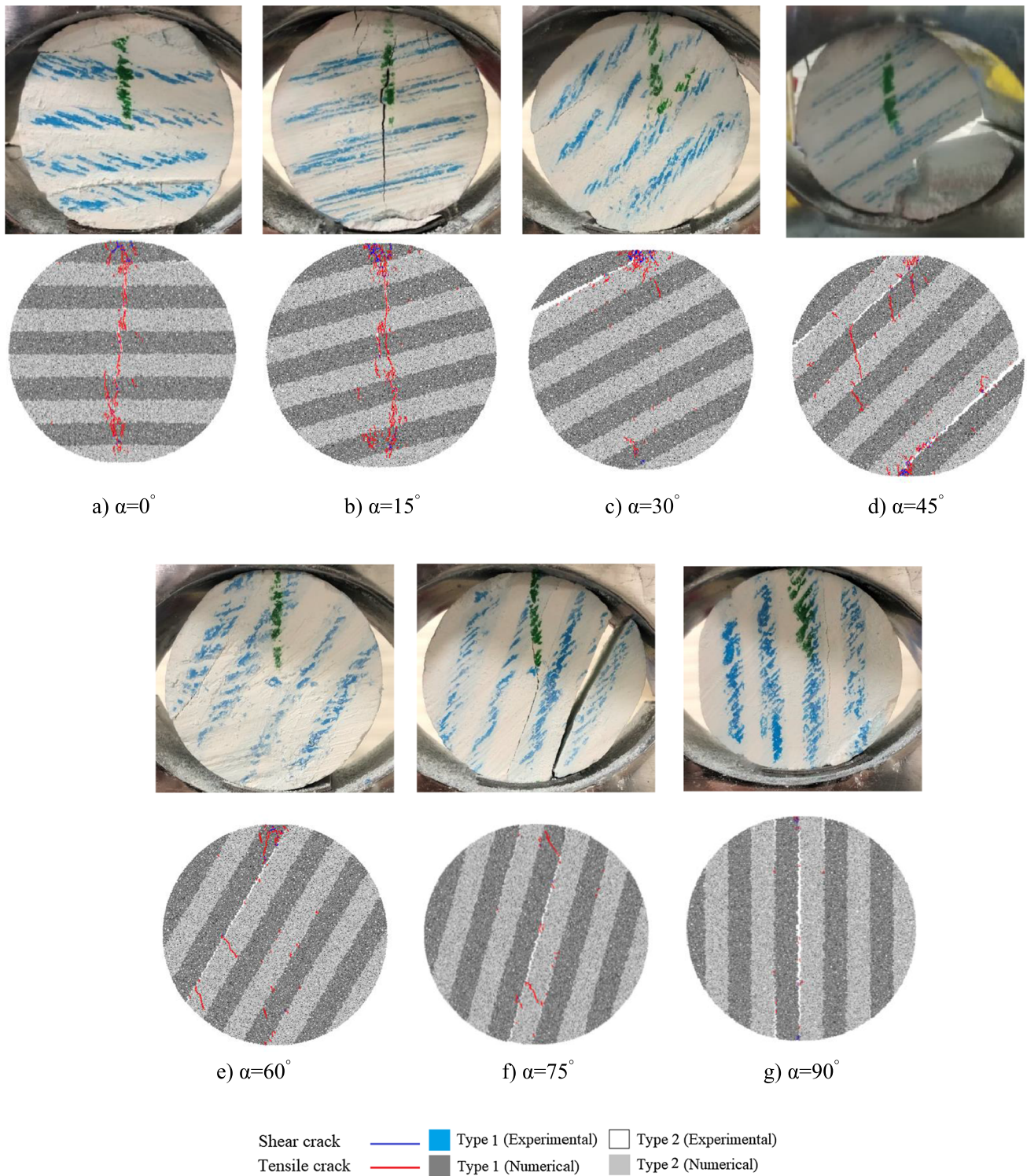| Shear crack | —— | ■ Type 1 (Experimental) | □ Type 2 (Experimental) |
| Tensile crack | —— | ■ Type 1 (Numerical) | ■ Type 2 (Numerical) |

**Fig. 8** Failure pattern of layered disks with $SR=0.1$

two layers, which was not discernible in the experimental specimens. When $\alpha=90°$, the central layer largely carried the axial load, which resulted in high compressive stress and a considerable number of tensile cracks (see Fig. 9g).

The fracture pattern of experimental samples closely resembles that of numerical ones. However, at $\alpha=15°$, two layers detached and moved towards the upper and lower parts of the specimen, while in the numerical specimens
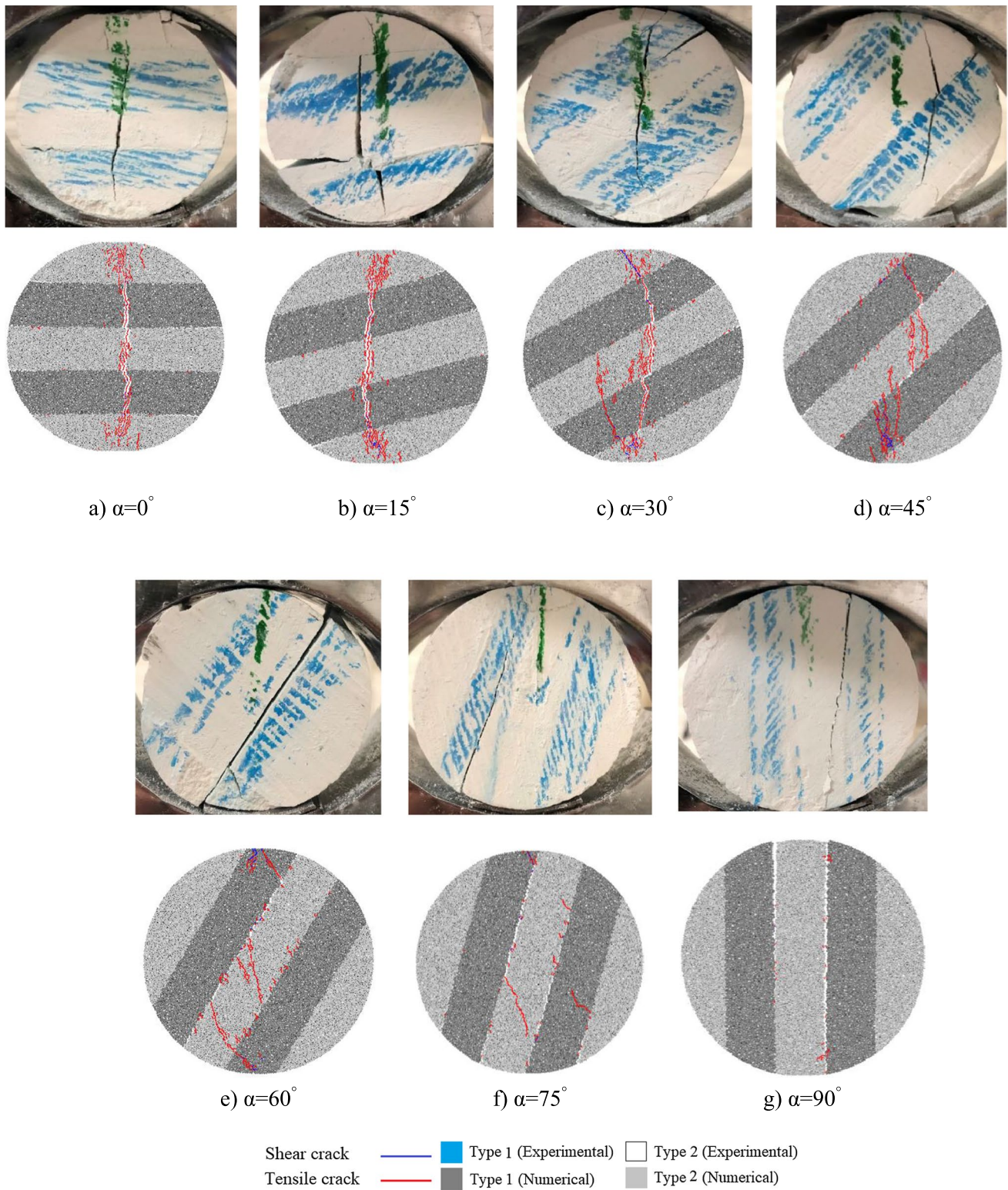
a) α=0°        b) α=15°        c) α=30°        d) α=45°



e) α=60°        f) α=75°        g) α=90°

| Shear crack | —— (blue) | ■ Type 1 (Experimental) | □ Type 2 (Experimental) |
| Tensile crack | —— (red) | ■ Type 1 (Numerical) | ▨ Type 2 (Numerical) |

**Fig. 9** Failure pattern of layered disks with $SR = 0.2$

(see Fig. 9a, b), the signs of detachment were observable only on the right side of the samples. Moreover, at $\alpha = 90°$ the split transpired along one bedding plane at the right side of the sample. However, in the numerical sample, many cracks formed at the contacts of the disk with the loading platens, mainly due to the buckling of the middle

a) α=0°        b) α=15°        c) α=30°        d) α=45°

e) α=60°        f) α=75°        g) α=90°

Shear crack ——— ■ Type 1 (Experimental)    □ Type 2 (Experimental)
Tensile crack ——— ■ Type 1 (Numerical)    ▨ Type 2 (Numerical)
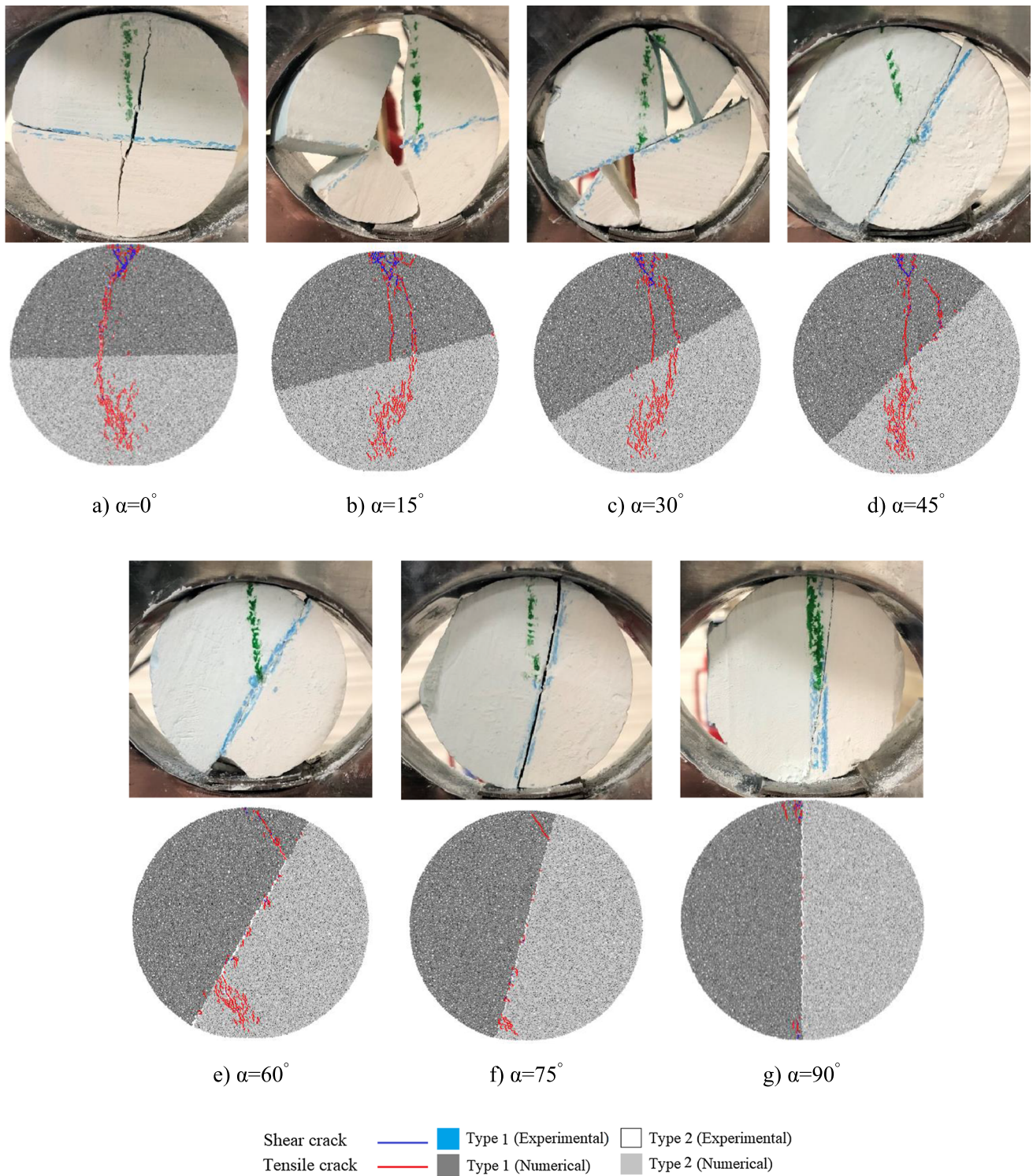
**Fig. 10** Failure pattern of layered disks with an of $SR = 0.5$

layer (see Fig. 9g). This phenomenon occurred as the layer was in direct contact with the platens, which imposed the entire applied load on this layer.

### 4.2.3 Disks with SR = 0.5

In experimental samples, especially for $\alpha < 45°$, *TL-PB* failure pattern developed. A tensile crack formed at the disk center, and a separation of layers occurred at the center too. However, in numerical models, separating the two layers did not occur, and samples failed in *TL* mode (See Fig. 10a, b, c and d).

Furthermore, in both methods, *PB* evolved in disks with $\alpha = 60°$, 75°, and 90° (see Figs. 13e, f, and g). In samples with an inclination angle of 60° and 75°, a minor fracture branched from the major fracture into the layers at both ends of the bedding plane, whereas for $\alpha = 90°$, a minor fracture, beginning from the contact with the lower platen, propagated in the strong layer and extend to near the disk center (see Fig. 10g).

## 4.3 Crack development analysis

### 4.3.1 Cracking process

The cracking processes, ultimately leading to the failure of the disks were thoroughly examined using numerical investigations (see Figs. 11, 12, 13). For disks with $SR = 0.1$, tensile cracks were mainly generated initially at the contact of the disks with the upper loading platen. When $\alpha = 0°$ and 15°, these cracks grew further along the disk centerline to reach the lower contact, dividing the disks into two halves. However, for higher values of $\alpha$, the separation of layers occurred. When $30° \leq \alpha \leq 75°$, sliding occurred along one bedding plane except for $\alpha = 45°$, in which sliding was observed along more bedding planes. Additionally, as sliding progressed, tensile cracks began to branch off from the bedding plane into the lower layers, inclined to the loading axis. For $\alpha = 90°$, cracks grew along the bedding plane, which coincided with the disk's vertical centerline, dividing the disk into two halves (see Fig. 11).

Moreover, when $SR = 0.2$ and $\alpha = 0°$ and 15°, crack formed initially in the stronger layers (Type 1), followed by cracks developing in the middle layer (Type 2). The cracks finally grew towards the contacts of the disks with the loading platens, separating the disks into two halves. This process was nearly similar to $\alpha = 30°$ and 45°. However, in these models, some cracks developed along part of the bedding planes, which connected the cracks growing through the layers. This cracking process ultimately divided the disks into two parts. For $\alpha > 45°$, sliding along the bedding planes of the middle Type 2 layer took place. However, when $\alpha = 60°$

and 75°, some cracks evolved largely through that layer, which was inclined towards the loading direction (Fig. 12).

Finally, for $SR = 0.5$ and $\alpha \leq 45°$, cracks mainly initiated at the contact of the Type 2 layer with the lower loading platen, and then they formed at the contact of the Type 1 layer with the upper loading platen. These cracks developed further towards the disk center, resulting in the specimens breaking into two halves. For $\alpha = 60°$ and 75°, cracks formed along the bedding plane, and at the final stages, those branched off the two ends of the plane, evolving towards the contacts with the loading platens. For these specimens, the two layers slide along the bedding plane. When $\alpha = 90°$, cracks developing along the bedding plane caused the disk to split (see Fig. 13).

It is worth mentioning that the cracking process of models where cracks initiate at the contacts of disks with loading platens resembled that of a non-layered rock specimen [7].

### 4.3.2 Number of cracks

Another significant factor that should be considered is the number of cracks forming in the disks. When rocks are loaded, two types of primary cracks may emerge, including shear and tensile cracks. During the numerical simulation, the number of each of the cracks was recorded for every disk. The variations in the number of cracks versus layer inclination angle ($\alpha$) are presented in Figs. 14–16. Although each group had its own specific trend, the most significant common feature among them is that the lowest number of cracks is generated at $\alpha = 90°$. Additionally, tensile cracks account for substantially the highest proportion of the total cracks created in the disks.

In specimens with $SR = 0.1$, the number of tensile cracks peaked at $\alpha = 15°$ before experiencing an abrupt decline at $\alpha = 30°$ (see Fig. 14). Then, it rose at $\alpha = 45°$, followed by a noticeable decrease at $\alpha = 90°$. In contrast, the trend for shear crack differed slightly, and its number peaked at 100 at $\alpha = 15°$ and fell continuously to nearly zero at $\alpha = 90$.

However, the number of shears and tensile cracks of disks with $SR = 0.2$ followed a different trend (see Fig. 15). The number of tensile cracks increased from about 700–1000 in $\alpha = 30°$ and remained constant at $\alpha = 45°$, followed by a considerable decline at $\alpha = 90°$ with 84 cracks. The figure for shear cracks followed the same trend as tensile cracks, with the highest value of around 200 and the lowest value of roughly zero at $\alpha = 90°$ and 75°, respectively.

Finally, for samples with $SR = 0.5$, the number of tensile cracks remained approximately unchanged at about 1000 between layer inclination angles of $\alpha = 0°$ and 45°, after which it dropped to well under 200 at $\alpha = 90°$. It should be noted that shear cracks followed a trend approximately similar to that of tensile cracks (see Fig. 16).

**Fig. 11** Failure process of layered disk samples with SR = 0.1
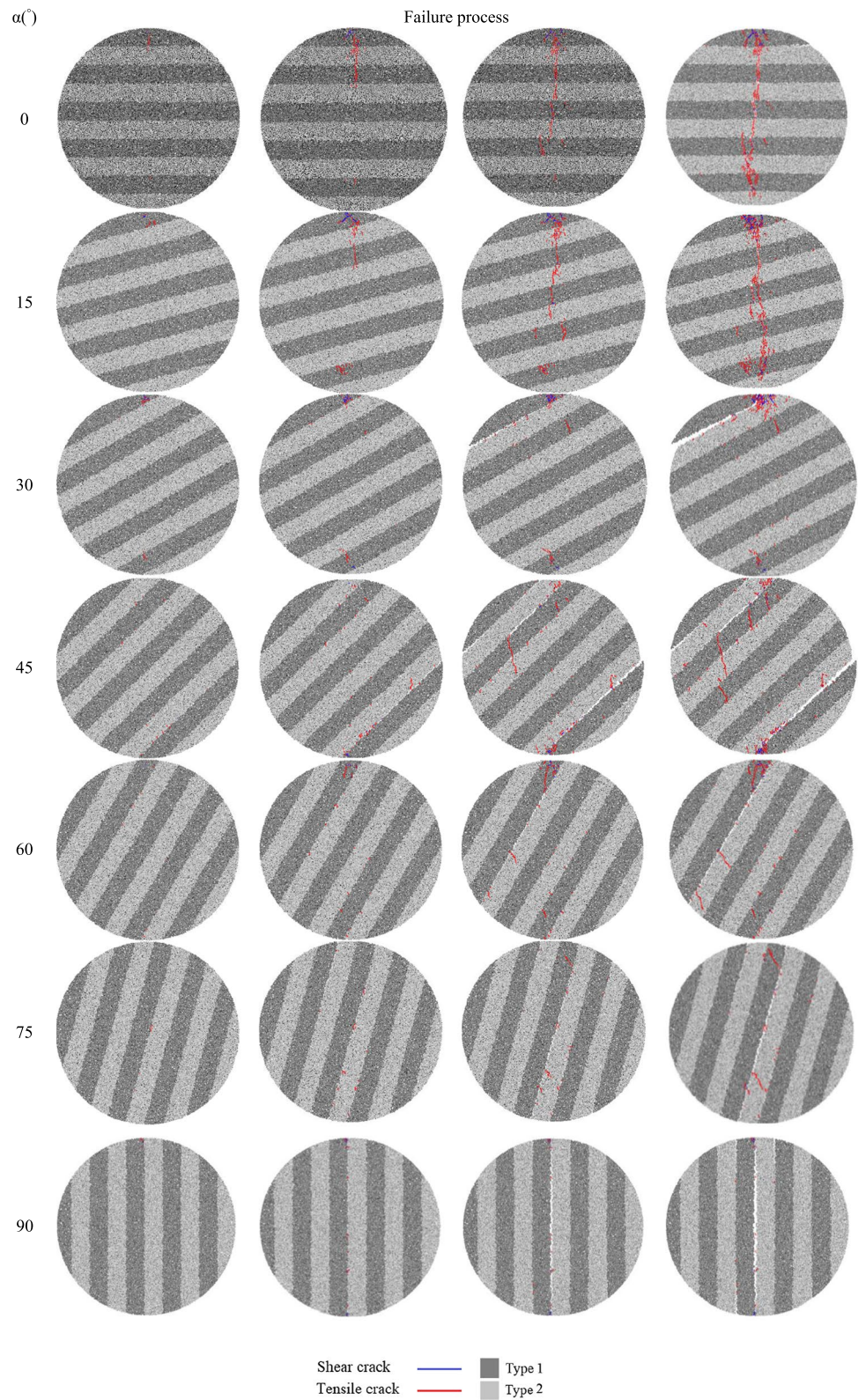
### 4.3.3 Crack orientation

The orientation of the cracks generated in the disks was evaluated using numerical simulations. Generally, shear cracks create a conjugate system, and tensile ones are nearly vertical (see Figs. 17–19). In these diagrams, a dip is measured from the positive x-direction pointing to the right of the specimens. The dip ranged from 0° to 180°. A dip equal

**Fig. 12** Failure process of layered disk samples with SR = 0.2

α(°)                                    Failure process



Shear crack ——— ▪ Type 1
Tensile crack ——— ▪ Type 2
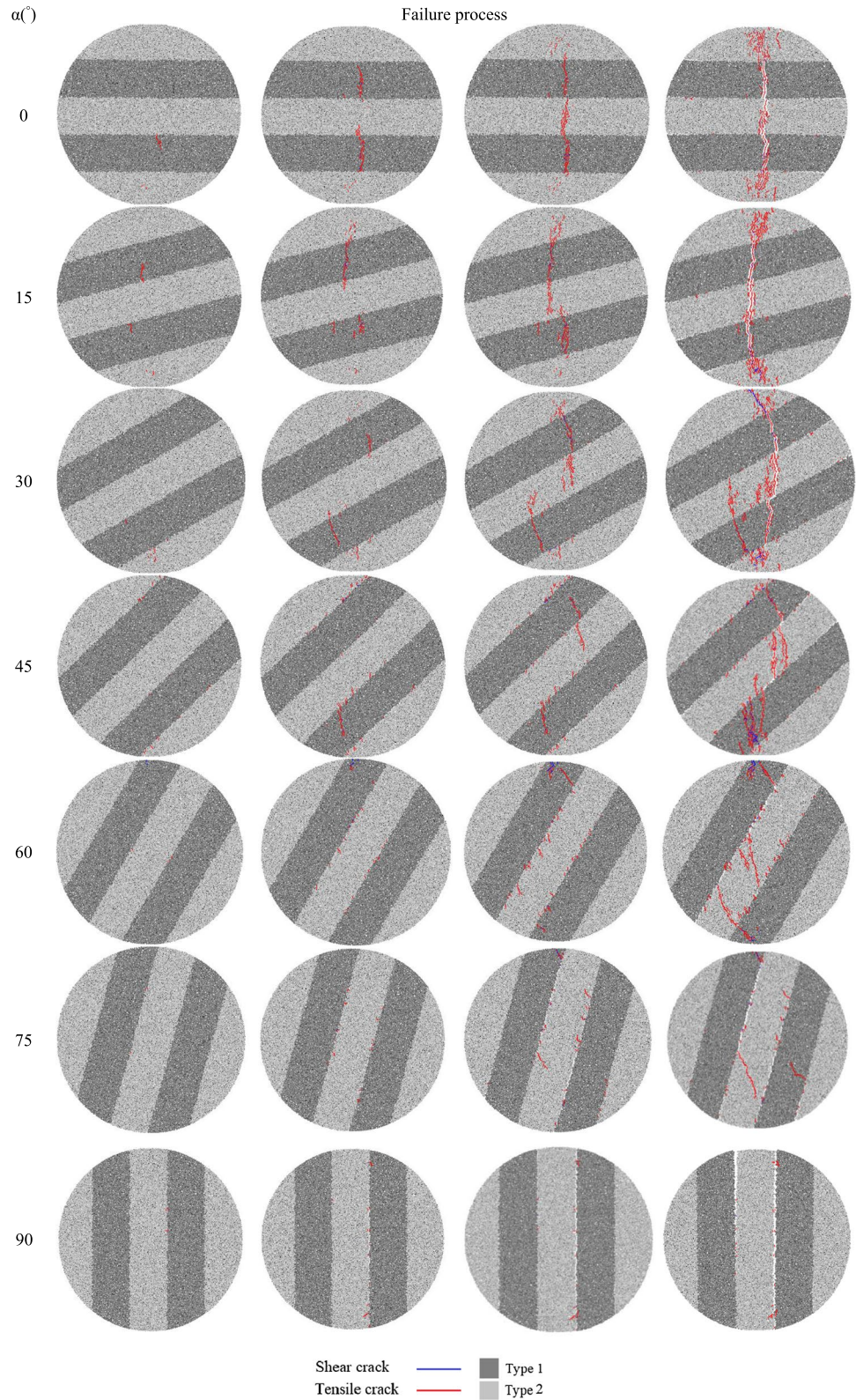
to 90° specifies vertical cracks, and 0° or 180° represent horizontal cracks in the disks. Additionally, cracks with dip ranging between 0° and 90° dip towards the right side of the disks and those having dip between 90° and 180° dip towards the left one and to obtain the true dip of these cracks, their dip on the diagrams need to be subtracted from

**Fig. 13** Failure process of layered disk samples with $SR = 0.5$
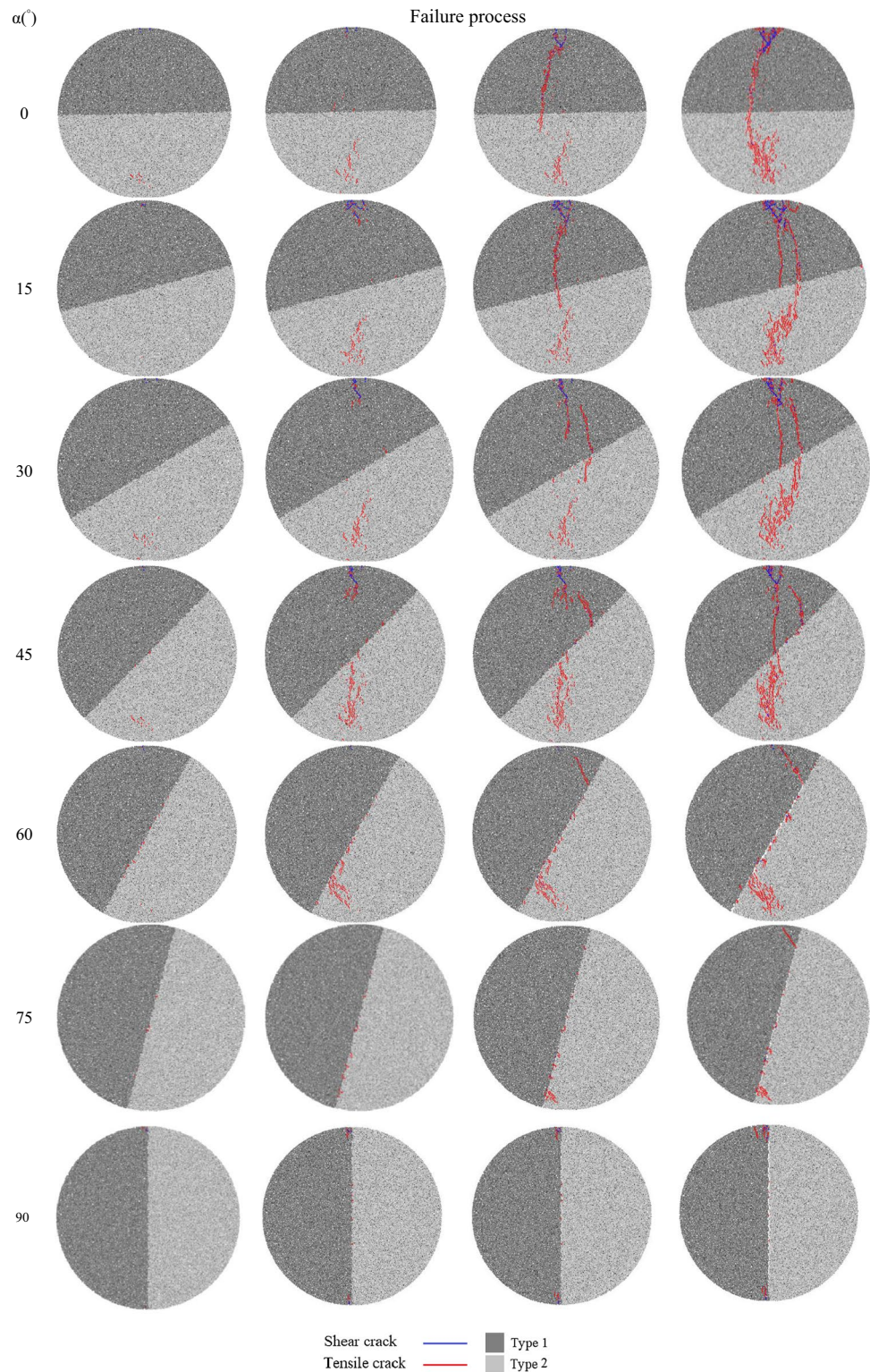


180°. In the following sections, crack orientation is examined thoroughly.

**4.3.3.1 i) Disks with SR = 0.1** As it can be seen from Fig. 17 (blue rosette diagrams), there was one dominant shear crack set for $\alpha$ ranging between 15° and 75°, whose dip was either less than 90° or equal to 140°. It is observed in the disks with a layer inclination angle of 15°, 30°, and 75° that the dip of the dominant crack sets was 40°, 60°, and 20°, respectively (see Fig. 17b, c, and f). When $\alpha = 45°$ and 60°, the dip

**Fig. 14** Variation in the number of shear and tensile cracks versus layer inclination in samples with $SR = 0.1$
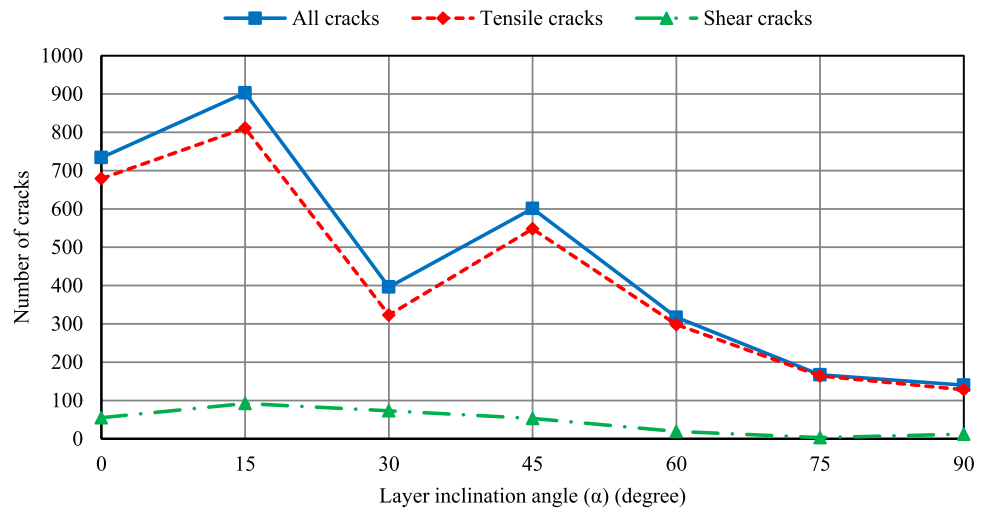


**Fig. 15** Variation in the number of shear and tensile cracks versus layer inclination in samples with $SR = 0.2$
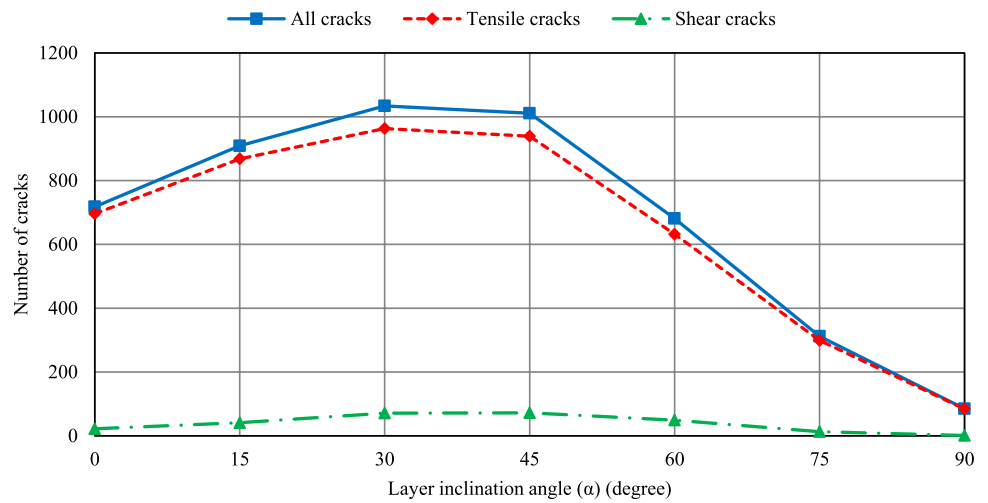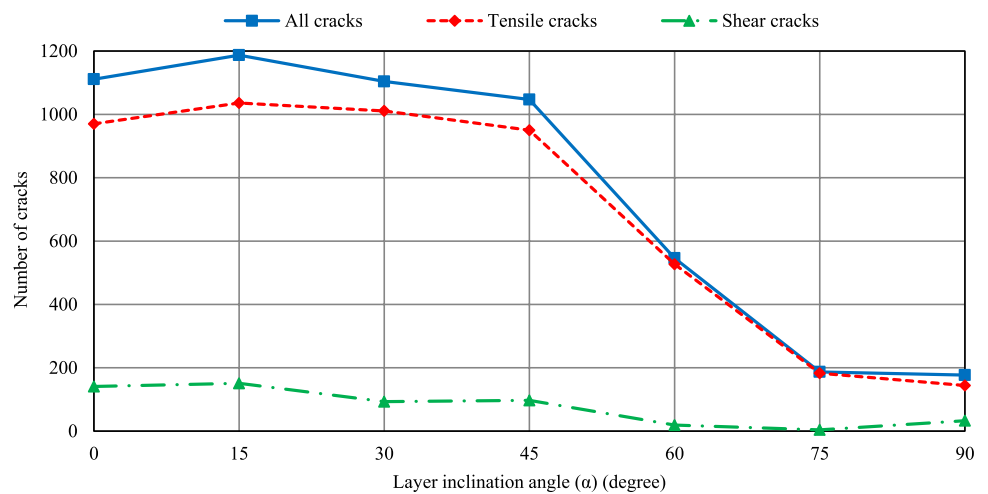


**Fig. 16** Variation in the number of shear and tensile cracks versus layer inclination in samples with $SR = 0.5$

a) α=0°                                                          b) α=15°

c) α=30°                                                          d) α=45°

e) α=60°                                                          f) α=75°
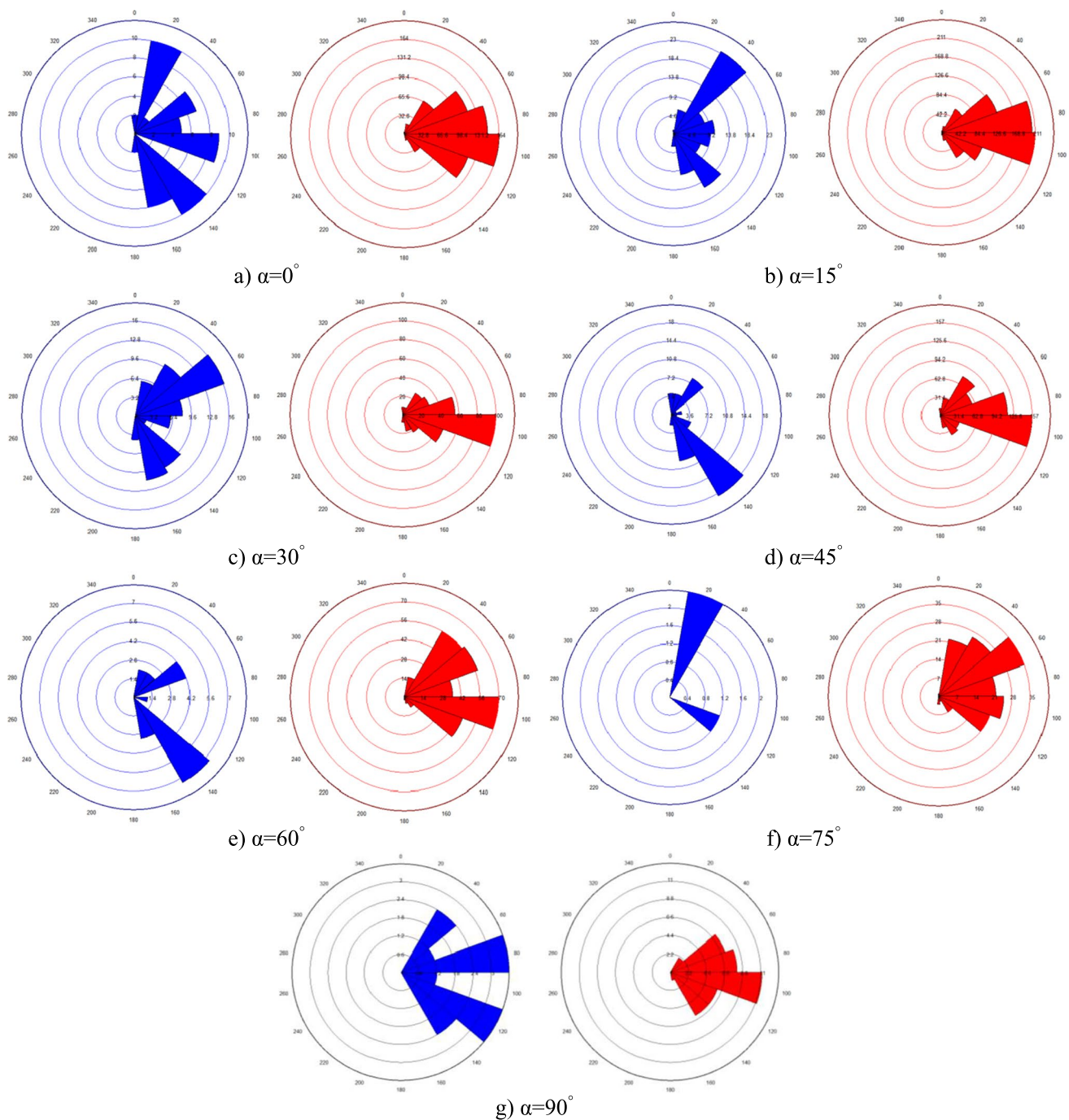
g) α=90°

**Fig. 17** Rosette diagrams for a disk with a spacing ratio of 0.1 ($SR=0.1$) at failure; blue: shear, red: tension (color figure online)

of the dominant crack set was 140° (see Figs. 17d, e, g). In the model with $\alpha=90°$, two major shear crack sets grew, dipping at 80° and 120°. However, when $\alpha=0°$, four major crack sets evolved with dips of 20°, 100°, 140°, and 160°. Note that crack sets with dips equal to 20° and 140° were the most frequently occurring cracks in the disks. Besides, in disks with $\alpha=0°$, 15°, and 30°, cracks evolved in more directions than in other disks.

As far as tensile cracks are concerned, they primarily had a dip ranging between 60° and 120° (see Fig. 17a, b, c, d, e, f, g). For $\alpha=15°$, predominant tensile crack sets dipped from 80° to 100°, while for $\alpha=0°$, 30°, 45°, 60°, and 90°, these cracks mainly grew at a dip equal to 100°. However, for the disk with $\alpha=75°$, the dip of the primary crack set was 60°, and most of the tensile cracks formed at a dip ranging between 20° and 120° (see Fig. 17, red rosette diagrams).
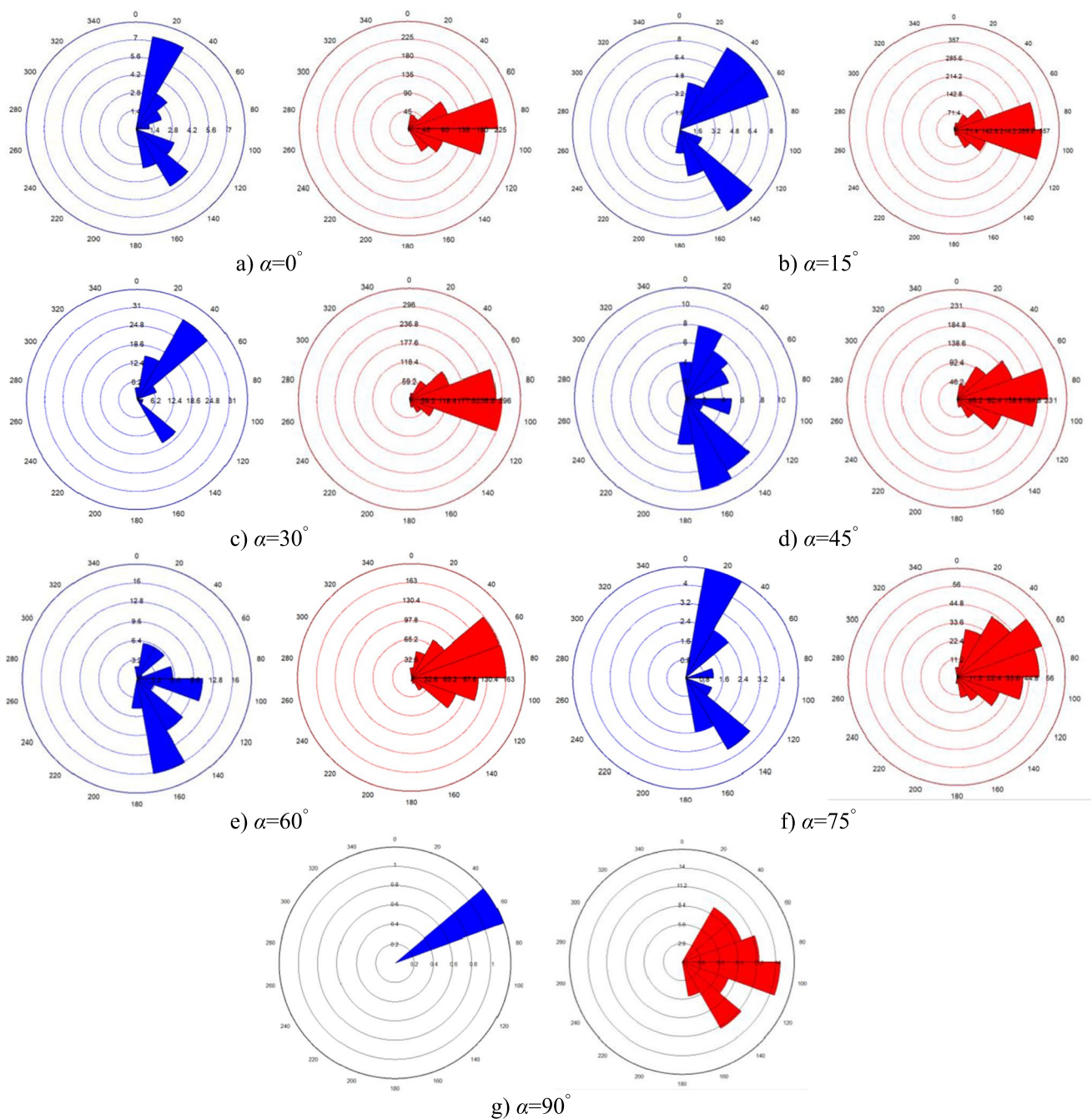
**Fig. 18** Rosette diagrams for the disk with a spacing ratio of 0.2 ($SR = 0.2$) at failure; blue: shear, red: tension (color figure online)

**4.3.3.2 *ii) Disks with SR = 0.2*** It is evident in Fig. 18 (blue rosette diagrams) that there was one major shear crack set for all the samples except for the disk with $\alpha = 15°$ in which three primary crack sets were created and for $\alpha = 90°$ where only one single shear crack occurred. The dip of the dominant set were 20° ($\alpha = 0°$ and 75°), 40° ($\alpha = 30°$), and 160° ($\alpha = 45°$ and 60°), while for $\alpha = 15°$, the dip of the dominant crack sets were 20°, 40°, and 140°. In addition, in samples

with $\alpha = 30°$, cracks developed in fewer dips than in other disks.

On the other hand, the red Rosette diagrams show that most of the tensile cracks propagated at dip ranging between 80° and 100° except for the disks with $\alpha = 65°$, 75°, and 90° (see Fig. 18, red rosette diagrams). For specimens with $\alpha = 0°$ and 45°, tensile cracks evolved predominantly at the dip of 80°, and for specimens with $\alpha = 15°$ and 30°, the dominant tensile crack set dipped at 100°. However, when

a) $\alpha=0°$

b) $\alpha=15°$

c) $\alpha=30°$

d) $\alpha=45°$
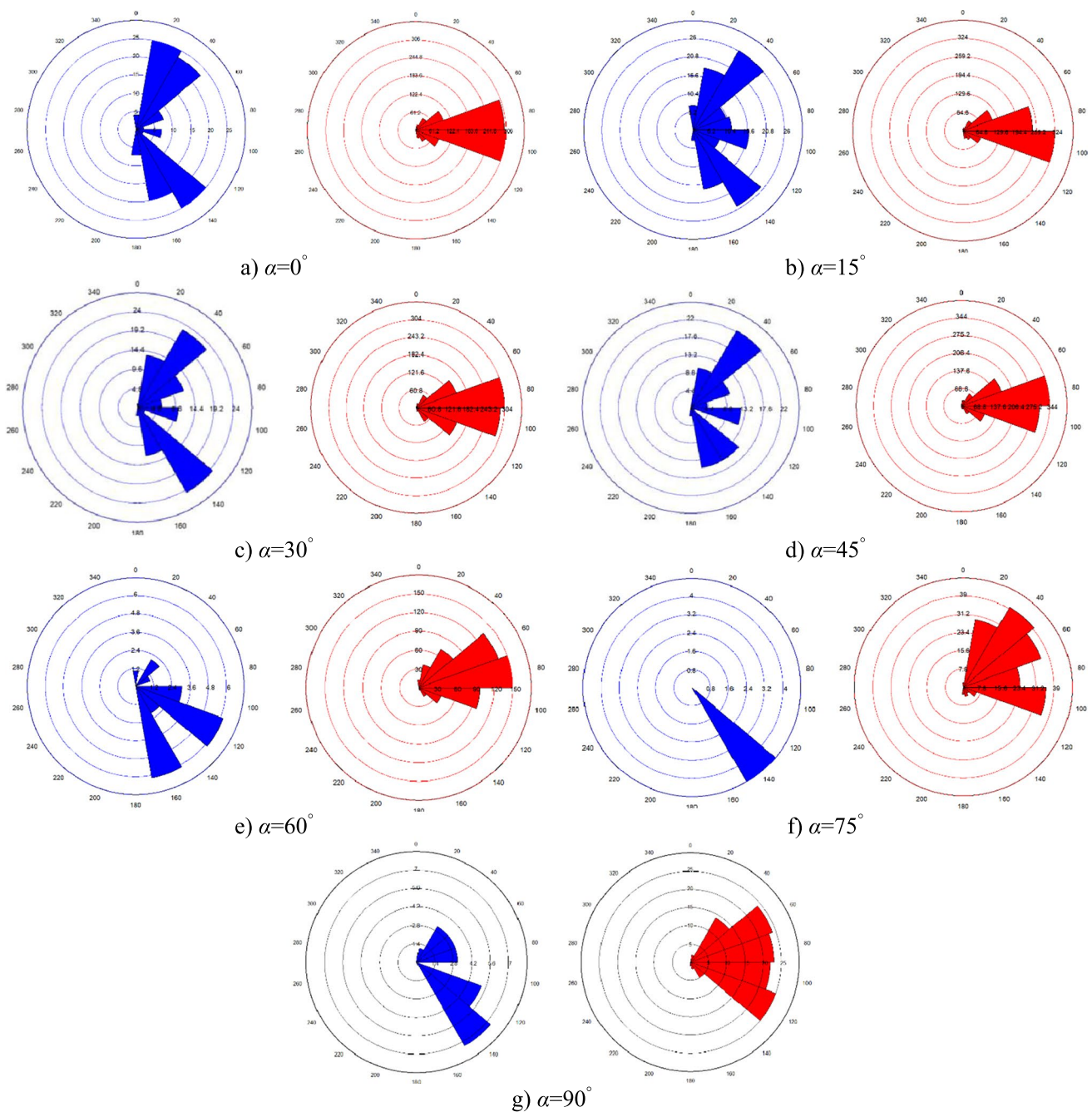
e) $\alpha=60°$

f) $\alpha=75°$

g) $\alpha=90°$

**Fig. 19** Rosette diagrams for the disk with a spacing ratio of 0.5 ($SR=0.5$) at failure; blue: shear, red: tension (color figure online)

$\alpha=60°$, two major crack sets dipping at 60°, and 80° developed. When the inclination angle was 75°, the cracks frequently evolved at dips ranging from 40° to 100°, and the predominant crack set had a dip equal to 60°. For $\alpha=90°$, the dip of tensile cracks ranged mainly from 40° to 140°, but they grew more frequently at 100° than the other dips.

**4.3.3.3 iii) Disks with SR=0.5** The blue rosette diagrams in Fig. 19 show that in specimens with $\alpha=0°$, 15°, 30°, and

60°, two dominant crack sets were generated. For $\alpha=0°$, these crack sets had a dip of 20° and 140° although those propagating with the dip of 40° and 160° were significant too. Moreover, for $\alpha=15°$ and 30°, the dip of the primary crack sets was 40° and 140°, while for $\alpha=60°$, the crack sets developed at dips of 120° and 160°. In contrast, one dominant crack set was observed in specimens with $\alpha=45°$, 75°, and 90°, dipping at 40° and 140° for the two latter. Note that for $\alpha=75°$, only one crack set propagated in the specimen.

As for tensile cracks, most of them formed at dips ranging between 80° and 100° which was not the case in the disks with $\alpha=75°$ (see Fig. 19, red rosette diagrams). For specimens with $\alpha=0°$, 30°, the dominant crack set was formed at a dip of both 80° and 100°. When $\alpha=15°$, tensile cracks predominantly developed at a dip of 100° while for $\alpha=45°$ and 60°, they largely dipped at 80°. However, the propagation of the dominant crack set in the disk with $\alpha=75°$ transpired mainly at a dip of 40°, although the number of cracks developed at other dips was moderately lower than that for the major set. Moreover, when $\alpha=90°$, tensile cracks mainly dipped between 60° and 120°, with slightly more cracks dipping at 120°.
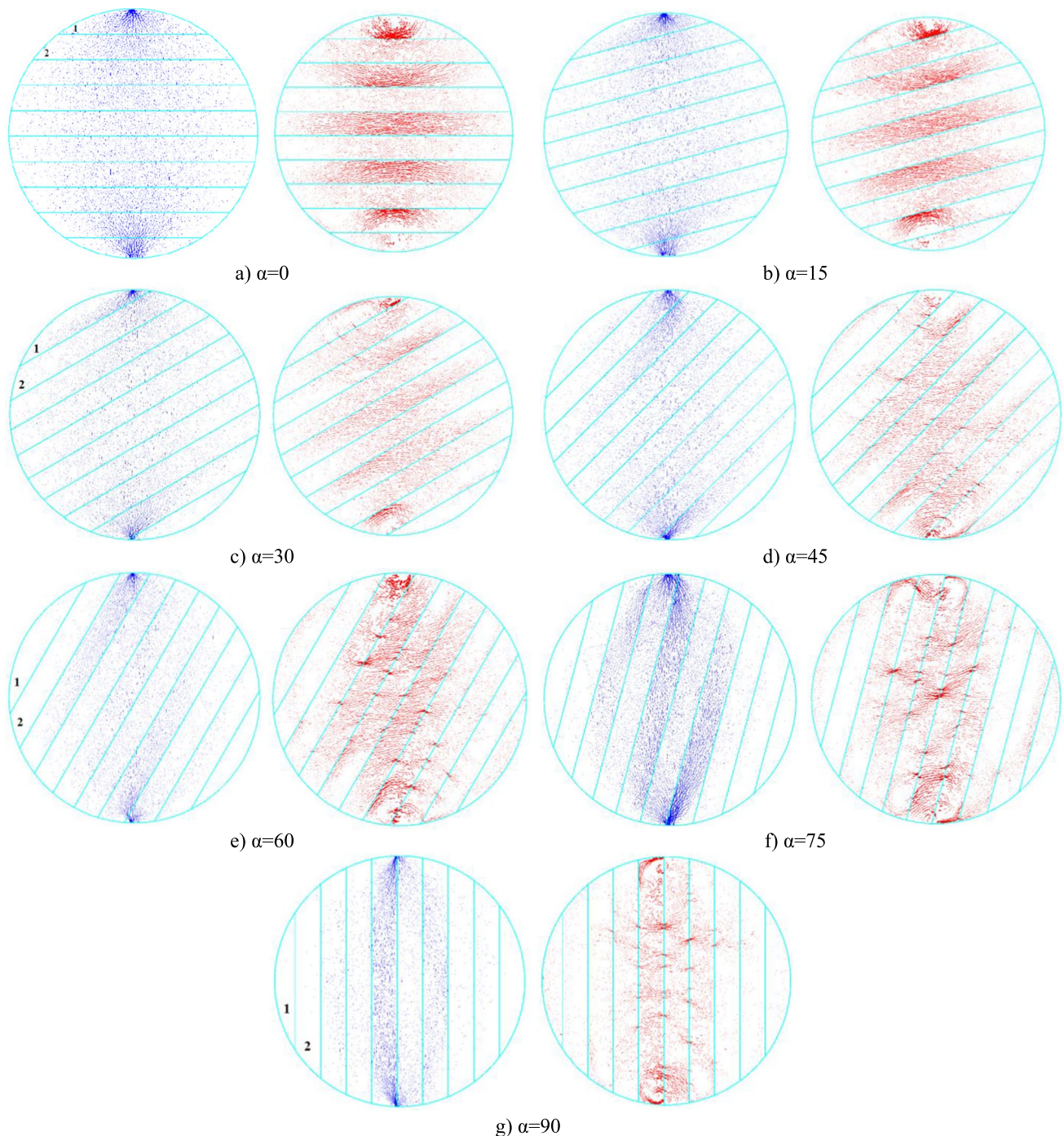


**Fig. 20** Force chain developed in disks with a spacing ratio of 0.1 (*SR=0.1*) at the initiation of the first crack; blue: compression, red: tension; 1: type 1, 2: type 2 (color figure online)

a) α=0

b) α=15

c) α=30

d) α=45
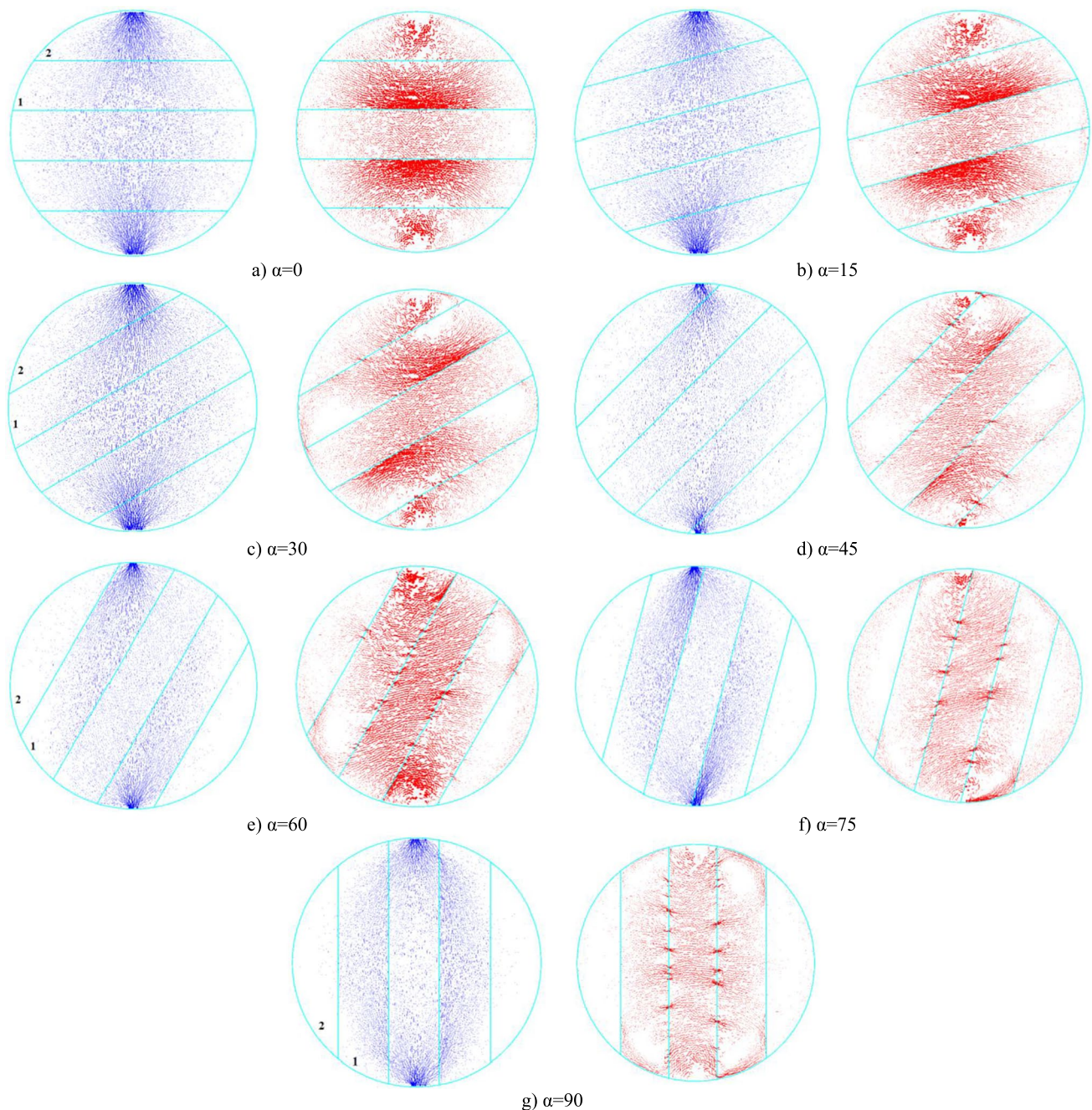
e) α=60

f) α=75

g) α=90

**Fig. 21** Force chain developed in disks with a spacing ratio of 0.2 (*SR=0.2*) at the initiation of the first crack; blue: compression, red: tension; 1: type 1, 2: type 2 (color figure online)

To sum up, it can be inferred from the tensile Rosette diagrams (see Figs. 17, 18, 19) that for $\alpha=0°$, 15, 30°, and 45°, the disks fractured nearly vertically, or in other words, through the layers. However, fractures inclined close to that of the layers in specimens with $\alpha \geq 60°$.

## 4.4 Contact force chain

The evolution of shear and tensile force chains in the disks with different spacing ratios (*SR*) and various layer inclination angles (*α*) just before the initiation of the first crack is shown in Figs. 20, 21 and 22. These figures revealed that when $\alpha < 45°$, compressive forces were distributed
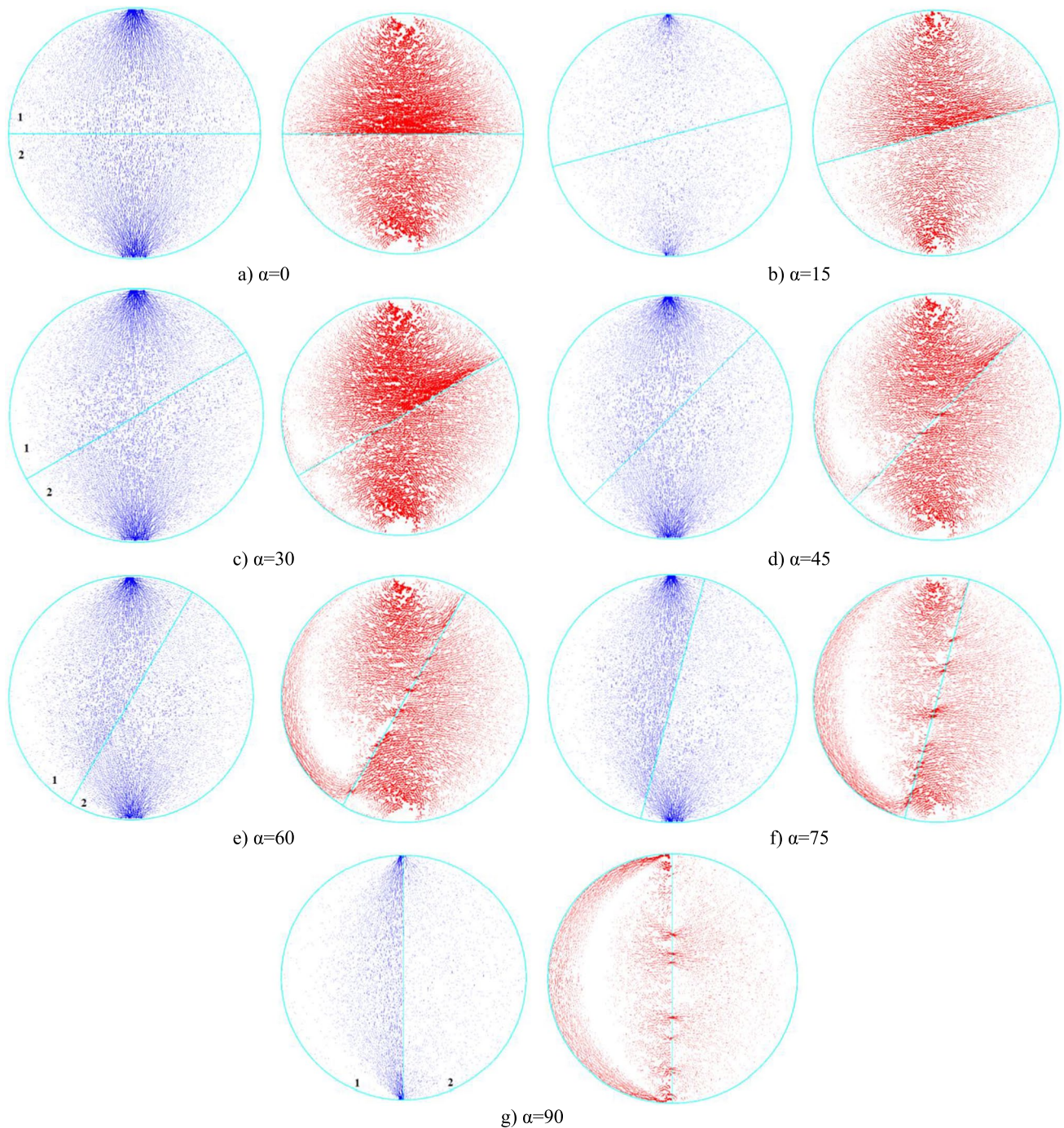
**Fig. 22** Force chain developed in disks with a spacing ratio of 0.5 (*SR=0.5*) at the initiation of the first crack; blue: compression, red: tension; 1: type 1, 2: type 2 (color figure online)

all over the disks and concentrated primarily at the contacts between the disks and loading jaws. However, when the spacing ratio was 0.1 or 0.2, and $\alpha = 45°$, these forces began to further concentrate in layers of Type 1 than in Type 2, and as $\alpha$ rises, the compressive forces tended to develop in stronger layers in the central part of the disk. Moreover, these forces were significantly directed to the layers of Type 1 that were either in direct contact with the loading jaws or adjoining the layer of Type 2 that had contact with the loading platens. Consequently, compressive forces barely developed in the side layers of the disks. A similar trend was identifiable for disks with a spacing ratio of 0.5, but since these disks consisted of only two layers, the trend was slightly different. As $\alpha$ exceeded 45°,

compressive forces in the Type 1 layer concentrated further along the layer plane, which led to virtually no compressive forces being distributed on its outer periphery. In addition, with the increase of layer inclination angle, tensile forces were just distributed in layers of Type 1 close to the disk centerline.1

In regards to the tensile force chains, when $\alpha$ ranged from 0° to 30°, tensile forces accumulated dramatically in layers of Type 1, although with the increase of $\alpha$ in this range, the concentration of these forces in these layers fell moderately (see Figs. 20, 21 and 22). In addition, the accumulation of tensile forces in the Type 1 layers rose around the vertical centerline of the disk and adjacent to the Type 2 layers that were closer to the disk center. As $\alpha$ varied from 45° to 90°, an area of highly concentrated tensile forces was created along the vertical disk centerline, and this area shrunk with the increase in $\alpha$. For disks with a spacing ratio of 0.5, when $\alpha$ changed between 45° and 90°, tensile forces began to develop along the bedding plane in the stronger layer, and the concentration of these forces on the outer perimeter of the layer of type 1 grew such that they developed over the entire outer perimeter of the layer for $\alpha = 90°$ (Fig. 22d, e, f and g).

# 5 Conclusion

In this paper, the impact of layer spacing ratio and inclination angle on tensile strength, crack development, failure pattern, and contact force chain of a layered disk under diametral loading was investigated using experimental and numerical approaches. PFC$^{2D}$ software was employed, and numerical models were calibrated and verified using experimental experiments. Finally, the numerical simulations were compared with experimental experiments, and the following conclusions were drawn:

- By increasing $\alpha$ from 0° to 90°, the tensile strength ($\sigma_{xx}$) of disks with different $SR$ peaked at $\alpha = 15°$ and then decreased, and as $SR$ increased from 0.1 to 0.5, the tensile strength increased. Moreover, as $\alpha$ and $SR$ increased, compressive stress ($\sigma_{yy}$) at the disk center broadly decreased, and its maximum was reached at $\alpha = 15°$ for $SR = 0.1$ and 0.5. However, in disks with $SR = 0.2$, $\sigma_{yy}$ peaked at $\alpha = 90°$ mainly due to the function of bearing capacity of the central layer. Shear stress ($\sigma_{xy}$) compared to the two other stress components was negligible; however, it peaked at $\alpha = 30°$ in all $SR$, and samples with $SR = 0.5$ had the maximum $\sigma_{xy}$.
- When $SR = 0.1$ and $\alpha < 30°$, the failure mode of both experimental and numerical models was primarily $TL$, and cracks developed along the disk centerline. However,

the inclination angle $PB$ failure mode was dominant for other layers. However, in numerical models, this pattern developed with some tensile cracks which were not identifiable in the experimental specimens. Moreover, for $SR = 0.2$, the numerical analysis showed that when $\alpha = 0°$ and 15°, the dominant failure pattern was $TL$ resulting in splitting of the disks in two halves, while for $\alpha = 30°$ and 45°, $TL$-$PB$ took place. The failure mode for $\alpha = 60°$, 75°, and 90° were considered as $PB$. Finally, when $SR = 0.5$ and $\alpha \leq 45°$, $TL$ and $TL$-$PB$ modes were responsible for the rupture of the numerical and experimental specimens, respectively.same For higher layer inclination angles, the specimens failed in $PB$ mode.

- In terms of crack development, for $SR = 0.1$ and 0.5, the maximum number of tensile cracks occurred at $\alpha = 15°$, whereas for $SR = 0.2$, this number peaked at $\alpha = 30°$. The number of shear cracks in comparison with tensile ones was negligible. Tensile cracks mainly developed in the direction of diametral loading, while the shear ones occurred in form of conjugate systems.
- The analysis of the contact force chain showed that virtually in all $SR$, when $\alpha \leq 30°$ tensile force concentrated in stronger layers more than the weaker ones, but at $\alpha > 30°$, this force was concentrated mainly around the disk centerline. However, in all $SR$, when $\alpha \leq 30°$, the bedding planes did not affect compressive force, which could quickly spread around the centerline; however, at $\alpha > 30°$, compressive force concentrated in stronger layers.

# Declarations

# References

1. Aadnoy, B., Looyeh, R.: Petroleum Rock Mechanics : Drilling Operations and Well Design, 2nd edn. Gulf Professional Publishing, Oxford (2011)
2. Abdullah, R., Tsutsumi, T., Amin, M.F.M., et al.: Evolution on deformation behaviour of brazilian test under different contact area using particle image velocimetry and finite element modelling. Measurement **159**, 107796 (2020). https://doi.org/10.1016/j.measurement.2020.107796
3. Al-Harthi, A.A.: Effect of planar structures on the anisotropy of Ranyah sandstone, Saudi Arabia. Eng. Geol. **50**, 49–57 (1998). https://doi.org/10.1016/S0013-7952(97)00081-1
4. Amadei, B.: Importance of anisotropy when estimating and measuring in situ stresses in rock. Int. J. Rock Mech. Min. Sci. Geomech. Abstr. **33**, 293–325 (1996). https://doi.org/10.1016/0148-9062(95)00062-3

5. Amir Hosseini, M., Kamrava, S., Sahimi, M., Tahmasebi, P.: Effect of wettability on two-phase flow through granular porous media: fluid rupture and mechanics of the media. Chem. Eng. Sci. **269**, 118446 (2023). https://doi.org/10.1016/J.CES.2023.118446

6. Asadizadeh, M., Khosravi, S., Karimi, J., et al.: Mechanical behavior of single-flawed cylindrical specimens subjected to axial loading: a numerical investigation. Bull. Eng. Geol. Environ. **81**, 442 (2022). https://doi.org/10.1007/s10064-022-02940-4

7. Bahaaddini, M., Serati, M., Masoumi, H., Rahimi, E.: Numerical assessment of rupture mechanisms in Brazilian test of brittle materials. Int. J. Solids Struct. **180–181**, 1–12 (2019). https://doi.org/10.1016/j.ijsolstr.2019.07.004

8. Bahaaddini, M., Sharrock, G., Hebblewhite, B.K.: Numerical investigation of the effect of joint geometrical parameters on the mechanical properties of a non-persistent jointed rock mass under uniaxial compression. Comput. Geotech. **49**, 206–225 (2013a). https://doi.org/10.1016/j.compgeo.2012.10.012

9. Bahaaddini, M., Sharrock, G., Hebblewhite, B.K.: Numerical direct shear tests to model the shear behaviour of rock joints. Comput. Geotech. **51**, 101–115 (2013b). https://doi.org/10.1016/j.compgeo.2013.02.003

10. Cai, M., Kaiser, P.: Numerical simulation of the Brazilian test and the tensile strength of anisotropic rocks and rocks with preexisting cracks. Int. J. Rock Mech. Min. Sci **41**, 478–483 (2004). https://doi.org/10.1016/j.ijrmms.2004.03.086

11. Chang, X., Zhao, H., Cheng, L.: Fracture propagation and coalescence at bedding plane in layered rocks. J. Struct. Geol. **141**, 104213 (2020). https://doi.org/10.1016/j.jsg.2020.104213

12. Chen, S., Yue, Z.Q., Tham, L.G.: Digital image-based numerical modeling method for prediction of inhomogeneous rock failure. Int. J. Rock Mech. Min. Sci. **41**, 939–957 (2004). https://doi.org/10.1016/J.IJRMMS.2004.03.002

13. Chen, S., Yue, Z.Q., Tham, L.G., Lee, P.K.K.: Modeling of the indirect tensile test for inhomogeneous granite using a digital image-based numerical method. Int. J. Rock Mech. Min. Sci. **41**, 466–471 (2004). https://doi.org/10.1016/J.IJRMMS.2004.03.084

14. Cho, J.-W., Kim, H., Jeon, S., Min, K.-B.: Deformation and strength anisotropy of Asan gneiss, Boryeong shale, and Yeoncheon schist. Int. J. Rock Mech. Min. Sci. **50**, 158–169 (2012). https://doi.org/10.1016/j.ijrmms.2011.12.004

15. Debecker, B., Vervoort, A.: Two-dimensional discrete element simulations of the fracture behaviour of slate. Int. J. Rock Mech. Min. Sci. **61**, 161–170 (2013). https://doi.org/10.1016/j.ijrmms.2013.02.004

16. Dorogoy, A., Banks-Sills, L.: Effect of crack face contact and friction on Brazilian disk specimens—a finite difference solution. Eng. Fract. Mech. **72**, 2758–2773 (2005). https://doi.org/10.1016/J.ENGFRACMECH.2005.05.005

17. Douma, L.A.N.R., Regelink, J.A., Bertotti, G., et al.: The mechanical contrast between layers controls fracture containment in layered rocks. J. Struct. Geol. **127**, 103856 (2019). https://doi.org/10.1016/j.jsg.2019.06.015

18. Duan, K., Kwok, C.Y.: Discrete element modeling of anisotropic rock under Brazilian test conditions. Int. J. Rock Mech. Min. Sci. **78**, 46–56 (2015). https://doi.org/10.1016/j.ijrmms.2015.04.023

19. Erarslan, N., Liang, Z.Z., Williams, D.J.: Experimental and numerical studies on determination of indirect tensile strength of rocks. Rock Mech. Rock Eng. **45**, 739–751 (2012). https://doi.org/10.1007/s00603-011-0205-y

20. Erarslan, N., Williams, D.J.: Experimental, numerical and analytical studies on tensile strength of rocks. Int. J. Rock Mech. Min. Sci. **49**, 21–30 (2012). https://doi.org/10.1016/j.ijrmms.2011.11.007

21. Feng, G., Kang, Y., Wang, X., et al.: Investigation on the failure characteristics and fracture classification of shale under Brazilian test conditions. Rock Mech. Rock Eng. **53**, 3325–3340 (2020). https://doi.org/10.1007/s00603-020-02110-6

22. He, J., Afolagboye, L.O.: Influence of layer orientation and interlayer bonding force on the mechanical behavior of shale under Brazilian test conditions. Acta Mech. Sin. **34**, 349–358 (2018). https://doi.org/10.1007/s10409-017-0666-7

23. Imani, M., Nejati, H.R., Goshtasbi, K.: Dynamic response and failure mechanism of Brazilian disk specimens at high strain rate. Soil Dyn. Earthq. Eng. **100**, 261–269 (2017). https://doi.org/10.1016/j.soildyn.2017.06.007

24. Imani, M., Nejati, H.R., Goshtasbi, K., Nazerigivi, A. Effect of brittleness on the micromechanical damage and failure pattern of rock specimens. Smart Struct. Syst. **29**(4), 535–547 (2022). https://doi.org/10.12989/SSS.2022.29.4.535

25. ISRM: The Complete ISRM Suggested Methods for Rock Characterization, Testing and Monitoring; 1974–2006, (2007)

26. Itasca Consulting Group Inc. PFC3D manual, (2022)

27. Khanlari, G., Rafiei, B., Abdilor, Y.: Evaluation of strength anisotropy and failure modes of laminated sandstones. Arab. J. Geosci. **8**, 3089–3102 (2015). https://doi.org/10.1007/s12517-014-1411-1

28. Khanlari, G., Rafiei, B., Abdilor, Y.: An experimental investigation of the Brazilian tensile strength and failure patterns of laminated sandstones. Rock Mech. Rock Eng. **48**, 843–852 (2015). https://doi.org/10.1007/s00603-014-0576-y

29. Lavrov, A., Vervoort, A.: Theoretical treatment of tangential loading effects on the Brazilian test stress distribution. Int. J. Rock Mech. Min. Sci. **39**, 275–283 (2002). https://doi.org/10.1016/S1365-1609(02)00010-2

30. Li, K., Cheng, Y., Yin, Z.-Y., et al.: Size effects in a transversely isotropic rock under brazilian tests: laboratory testing. Rock Mech. Rock Eng. (2020). https://doi.org/10.1007/s00603-020-02058-7

31. Lin, H., Cao, P., Wang, Y.: Numerical simulation of a layered rock under triaxial compression. Int. J. Rock Mech. Min. Sci. **60**, 12–18 (2013). https://doi.org/10.1016/j.ijrmms.2012.12.027

32. Liu, W.C., Tien, Y.M., Juang, C.H.: Numerical simulation for layered rock under Brazilian test. (2012)

33. Markides, C.F., Pazis, D.N., Kourkoulis, S.K.: (2010) Influence of friction on the stress field of the Brazilian tensile test. Rock Mech. Rock Eng. **441**(44), 113–119 (2010). https://doi.org/10.1007/S00603-010-0115-4

34. Mokhtari, M., Tutuncu, A.N.: Impact of laminations and natural fractures on rock failure in Brazilian experiments: a case study on green river and niobrara formations. J. Nat. Gas. Sci. Eng. **36**, 79–86 (2016). https://doi.org/10.1016/j.jngse.2016.10.015

35. Park, B., Min, K.-B.: Bonded-particle discrete element modeling of mechanical behavior of transversely isotropic rock. Int. J. Rock Mech. Min. Sci. **76**, 243–255 (2015). https://doi.org/10.1016/j.ijrmms.2015.03.014

36. Park, B., Min, K.-B., Thompson, N., Horsrud, P.: Three-dimensional bonded-particle discrete element modeling of mechanical behavior of transversely isotropic rock. Int. J. Rock Mech. Min. Sci. **110**, 120–132 (2018). https://doi.org/10.1016/j.ijrmms.2018.07.018

37. Pierce, M., Cundall, P., Potyondy, D., Mas Ivars, D.: A synthetic rock mass model for jointed rock. In: Proceedings of the first CA–US rock mechanics symposium, Vancouver, BC. pp 341–349, (2007)

38. Potyondy, D.O.: A flat-jointed bonded-particle material for hard rock. In: 46th US Rock Mechanics/Geomechanics Symposium 2012. pp 1510–1519, (2012)

39. Potyondy, D.O., Cundall, P.A.: A bonded-particle model for rock. Int. J. Rock Mech. Min. Sci. **41**, 1329–1364 (2004). https://doi.org/10.1016/j.ijrmms.2004.09.011

40. Pros, A., Díez, P., Molins, C.: Numerical modeling of the double punch test for plain concrete. Int. J. Solids Struct. **48**, 1229–1238 (2011). https://doi.org/10.1016/j.ijsolstr.2011.01.006

41. Serati, M., Bahaaddini, M., Roshan, H., et al.: On assessing the tensile cracking pattern in brittle rocks and solids. Bull. Eng. Geol. Environ. **80**, 5867–5879 (2021). https://doi.org/10.1007/s10064-021-02249-8

42. Serati, M., Masoumi, H., Williams, D.J., Alehossein, H.: Modified Brazilian test for indirect measurement of tensile strength of brittle materials. In: 51st U.S. Rock Mech. Symp. ARMA-2017–0834. (2017)

43. Shabani, F., Kaviani-Hamedani, F.: Cyclic response of sandy subsoil layer under traffic-induced principal stress rotations: Application of bidirectional simple shear apparatus. Soil Dyn. Earthq. Eng. **164**(2022), 107573 (2023). https://doi.org/10.1016/j.soildyn.2022.107573

44. Sun, W., Wu, S., Zhou, Y., Zhou, J.: Comparison of crack processes in single-flawed rock-like material using two bonded–particle models under compression. Arab. J. Geosci. **12**, 156 (2019). https://doi.org/10.1007/s12517-019-4327-y

45. Tan, X., Konietzky, H., Frühwirt, T., Dan, D.Q.: Brazilian tests on transversely isotropic rocks: laboratory testing and numerical simulations. Rock Mech. Rock Eng. **48**, 1341–1351 (2015). https://doi.org/10.1007/s00603-014-0629-2

46. Tavallali, A., Vervoort, A.: Failure of layered sandstone under Brazilian Test conditions: effect of micro-scale parameters on macro-scale behaviour. Rock Mech. Rock Eng. **43**, 641–653 (2010). https://doi.org/10.1007/s00603-010-0084-7

47. Tavallali, A., Vervoort, A.: Behaviour of layered sandstone under Brazilian test conditions: layer orientation and shape effects. J. Rock Mech. Geotech. Eng. **5**, 366–377 (2013). https://doi.org/10.1016/j.jrmge.2013.01.004

48. Tavallali, A., Vervoort, A.: Effect of layer orientation on the failure of layered sandstone under Brazilian test conditions. Int. J. Rock Mech. Min. Sci. **47**, 313–322 (2010). https://doi.org/10.1016/j.ijrmms.2010.01.001

49. Vervoort, A., Min, K.-B., Konietzky, H., et al.: Failure of transversely isotropic rock under Brazilian test conditions. Int. J. Rock Mech. Min. Sci. **70**, 343–352 (2014). https://doi.org/10.1016/j.ijrmms.2014.04.006

50. Wang, P., Cai, M., Ren, F.: Anisotropy and directionality of tensile behaviours of a jointed rock mass subjected to numerical Brazilian tests. Tunn. Undergr. Sp. Technol. **73**, 139–153 (2018). https://doi.org/10.1016/j.tust.2017.12.018

51. Wang, Z., Yang, S., Tang, Y.: Mechanical behavior of different sedimentary rocks in the Brazilian test. Bull. Eng. Geol. Environ. **79**, 5415–5432 (2020). https://doi.org/10.1007/s10064-020-01906-8

52. Xu, G., Gutierrez, M., He, C., Meng, W.: Discrete element modeling of transversely isotropic rocks with non-continuous planar fabrics under Brazilian test. Acta Geotech. **15**, 2277–2304 (2020). https://doi.org/10.1007/s11440-020-00919-7

53. Xu, G., He, C., Chen, Z., Wu, D.: Effects of the micro-structure and micro-parameters on the mechanical behaviour of transversely isotropic rock in Brazilian tests. Acta Geotech. **13**, 887–910 (2018). https://doi.org/10.1007/s11440-018-0636-7

54. Yang, S.-Q., Yin, P.-F., Huang, Y.-H.: Experiment and discrete element modelling on strength, deformation and failure behaviour of shale under Brazilian compression. Rock Mech. Rock Eng. **52**, 4339–4359 (2019). https://doi.org/10.1007/s00603-019-01847-z

55. Yang, S.Q., Huang, Y.H.: Particle flow study on strength and meso-mechanism of Brazilian splitting test for jointed rock mass. Acta Mech. Sin. Xuebao **30**, 547–558 (2014). https://doi.org/10.1007/s10409-014-0076-z

56. Yin, P.-F., Yang, S.-Q.: Experimental investigation of the strength and failure behavior of layered sandstone under uniaxial compression and Brazilian testing. Acta Geophys. **66**, 585–605 (2018). https://doi.org/10.1007/s11600-018-0152-z

57. Yu, J., Shang, X., Wu, P.: Influence of pressure distribution and friction on determining mechanical properties in the Brazilian test: theory and experiment. Int. J. Solids Struct. **161**, 11–22 (2019). https://doi.org/10.1016/j.ijsolstr.2018.11.002

58. Yu, Y., Yin, J., Zhong, Z.: Shape effects in the Brazilian tensile strength test and a 3D FEM correction. Int. J. Rock. Mech. Min. Sci. **43**, 623–627 (2006)

59. Yu, Y., Zhang, J., Zhang, J.: A modified Brazilian disk tension test. Int. J. Rock Mech. Min. Sci. **46**, 421–425 (2009). https://doi.org/10.1016/j.ijrmms.2008.04.008

60. Zhao, N.N., Feng, J.L.: Investigation on fracture mechanism of layered slate: experiment and beam-particle method. Environ. Earth Sci. **80**, 788 (2021). https://doi.org/10.1007/s12665-021-10106-w

61. Zhu, W.C., Tang, C.A.: Numerical simulation of Brazilian disk rock failure under static and dynamic loading. Int. J. Rock Mech. Min. Sci. **43**, 236–252 (2006). https://doi.org/10.1016/J.IJRMMS.2005.06.008